

# High-throughput sequencing of macaque basolateral amygdala projections reveals dissociable connectional motifs with frontal cortex

**Authors:** Zachary R Zeisler<sup>1</sup>, Liza London<sup>1</sup>, William G Janssen<sup>1,2</sup>, J Megan Fredericks<sup>1</sup>, Catherine Elorette<sup>1</sup>, Atsushi Fujimoto<sup>1</sup>, Huiqing Zhan<sup>5</sup>, Brian E Russ<sup>1,3,4</sup>, Roger L Clem<sup>1</sup>, Patrick R Hof<sup>1</sup>, Frederic M Stoll<sup>1</sup>, and Peter H Rudebeck<sup>1\*</sup>

## Author affiliations:

1. Nash Family Department of Neuroscience and Friedman Brain Institute, Icahn School of Medicine at Mount Sinai, One Gustave L. Levy Place, New York, NY 10029
2. Microscopy and Advanced Bioimaging CoRE, Icahn School of Medicine at Mount Sinai, One Gustave L. Levy Place, New York, NY 10029
3. Center for Biomedical Imaging and Neuromodulation, Nathan Kline Institute, 140 Old Orangeburg Road, 10 Orangeburg, NY 10962
4. Department of Psychiatry, New York University at Langone, One, 8 Park Ave, New York, NY 10016
5. Cold Spring Harbor Laboratory, 1 Bungtown Rd, Syosset, NY 11791

\*Corresponding author

## Correspondence should be addressed to:

Dr. Peter Rudebeck – [peter.rudebeck@mssm.edu](mailto:peter.rudebeck@mssm.edu)  
Nash Family Department of Neuroscience  
Icahn School of Medicine at Mount Sinai  
One Gustave L. Levy Place  
New York, NY 10029

**Author Contributions:** ZRZ, RLC, PRH, FMS, and PHR conceived the project. ZRZ and PHR designed and carried out the experiments, performed the analyses, and wrote the paper. LL performed the stereology analysis, WGJ assisted in tissue preparation, JMF assisted in surgery, CE and AF collected the fMRI scans, HZ performed the RNA extraction and sequencing, and BER performed the fMRI preprocessing and analysis. RLC, PRH, and FMS provided vital feedback on analysis approaches throughout. All authors approved the final version of the paper.

**Acknowledgements:** ZRZ, RLC, PRH, and PHR are supported by a grant from the BRAIN initiative (R34NS122050). We thank Allison Sowa of the ISMMS Microscopy and Advanced Bioimaging CoRE for help with tissue preparation, members of the Rudebeck Lab for assistance with surgical procedures, and the MAPseq Core at CSHL for assistance in tissue processing and sequencing. We also thank Anthony Zador and Alex Vaughan for advice and encouragement and Elisabeth Murray for comments on an earlier version of the manuscript.

## Abstract

The basolateral amygdala (BLA) projects widely across the macaque frontal cortex<sup>1-4</sup>, and amygdalo-frontal projections are critical for optimal emotional responding<sup>5</sup> and decision-making<sup>6</sup>. Yet, little is known about the single-neuron architecture of these projections: namely, whether single BLA neurons project to multiple parts of the frontal cortex. Here, we use MAPseq<sup>7</sup> to determine the projection patterns of over 3000 macaque BLA neurons. We found that one-third of BLA neurons have two or more distinct targets in parts of frontal cortex and of subcortical structures. Further, we reveal non-random structure within these branching patterns such that neurons with four targets are more frequently observed than those with two or three, indicative of widespread networks. Consequently, these multi-target single neurons form distinct networks within medial and ventral frontal cortex consistent with their known functions in regulating mood and decision-making. Additionally, we show that branching patterns of single neurons shape functional networks in the brain as assessed by fMRI-based functional connectivity. These results provide a neuroanatomical basis for the role of the BLA in coordinating brain-wide responses to valent stimuli<sup>8</sup> and highlight the importance of high-resolution neuroanatomical data for understanding functional networks in the brain.

## Introduction

1 Basolateral amygdala (BLA) is essential for adaptive emotional responding in humans  
2 and animals<sup>5,9,10</sup>. In humans, dysfunction within or damage to the circuits that connect through  
3 the amygdala are theorized to be the cause of numerous psychiatric disorders, including autism  
4 spectrum disorder, post-traumatic stress disorder, and schizophrenia<sup>11-13</sup>. Based on decades of  
5 tract-tracing studies in macaques, we know that the primate BLA projects widely across the  
6 brain, sending connections primarily to ventral and medial parts of the frontal lobe, as well as  
7 the temporal and occipital cortices, thalamus, and striatum<sup>1-4</sup>. These diverse and widespread  
8 connections, especially those to the frontal lobe, are central to accounts of how BLA in humans  
9 coordinates learning about and responding to different emotionally salient events<sup>14,15</sup>.

10 Despite the appreciation that the BLA plays a central role in coordinating activity across  
11 large networks to guide emotional behavior, the anatomical organization of single neuron  
12 connections from this area are largely unknown. One possibility is that single BLA neurons  
13 project to only one specific target, transmitting information to downstream targets in dedicated  
14 pathways. Such an organizing principle or connectional motif would align closely with the BLA's  
15 known role in model-based behaviors and the processing of sensory-specific stimuli through  
16 interaction with distinct parts of frontal cortex<sup>16,17</sup>. An alternative is that single neurons in BLA  
17 branch to many different areas, such that activity can be efficiently coordinated across  
18 distributed networks of areas. This organization fits with the BLA's role in more general aspects  
19 of motivation and response invigoration to approach or avoid salient stimuli that are  
20 characteristic of model-free behaviors<sup>8</sup>.

21 These two potential connectional motifs of single BLA neurons – specific vs branching –  
22 are not necessarily mutually exclusive. However, at present, the extent to which either motif  
23 best characterizes the projections of single BLA neurons or indeed populations of BLA neurons  
24 is not known, in part because gold-standard tract-tracing approaches are either too coarse to  
25 detect the projection patterns of individual neurons<sup>18,19</sup> or because the available single-axon  
26 tracing techniques do not scale practically to non-human primates<sup>20</sup>. To surmount these issues,  
27 we optimized and refined a high-throughput sequencing approach, multiplexed analysis of  
28 projections by sequencing (MAPseq<sup>7</sup>) in macaque monkeys. MAPseq uses barcoded mRNA

29 technology<sup>21</sup> to map the connections of individual neurons at scale. Because of their potential  
30 importance in psychiatric disorders<sup>11</sup>, we focused on projections from BLA to frontal cortex,  
31 striatum, anterior temporal lobe, and mediodorsal nucleus of the thalamus (MD), a part of  
32 thalamus that receives input from both frontal cortex and amygdala<sup>1</sup>. Using this approach, we  
33 found that individual BLA neurons project widely in frontal cortex; about half of the neurons  
34 that leave amygdala project to more than one target area. The pattern of these branching  
35 projections was not random, such that the connections of single neurons were organized into  
36 distinct and reproducible connection motifs. Notably, BLA projections to posterior parts of  
37 frontal cortex were highly specific, whereas those to more anterior parts of frontal cortex,  
38 especially ventral frontal cortex, were more likely to branch to multiple areas.

## 39 Results

### 40 Optimization of MAPseq in macaques

41 MAPseq<sup>7</sup> relies on an engineered sindbis virus that infects neurons with unique RNA  
42 sequences, referred to as barcodes<sup>21</sup>. Following viral expression these barcodes are conjugated  
43 to a nonfunctional presynaptic protein and undergo anterograde axonal transport. Thus, by  
44 dissecting and sequencing samples from injection and target brain areas, the projection  
45 patterns of single neurons can be determined. MAPseq thereby complements and extends  
46 traditional neuroanatomical approaches, as it provides both information about bulk projection  
47 patterns from one area to another as well as the connection patterns of single neurons.  
48 Further, it permits simultaneous analysis of projections to many target areas within the same  
49 animal, allowing single-neuron branching to be discerned.

50 We performed bilateral, MRI-guided stereotactic injections of barcoded sindbis virus  
51 into the BLA of two rhesus macaques (**Figure 1A**, see Extended Data Figure 1 for more detail);  
52 10 to 12 injections of 400 nl each were placed throughout the lateral, basal, and accessory basal  
53 nuclei to control viral spread. Following perfusion, brains were extracted, the hemispheres  
54 separated and sectioned. The BLA and target areas in frontal cortex, striatum, entorhinal  
55 cortex, hippocampus, and MD were dissected according to gray/white matter boundaries as  
56 well as sulcal landmarks (**Figure 1B**). Simple qPCR on extracted mRNA recovered significantly

57 more barcode in amygdala sites near the injection compared to target sites (OLS regression,  $t(2)$   
58 = 46.43,  $p < 0.0001$ ) and more in target sites compared to control sites in cerebellum ( $t(2) =$   
59 4.77,  $p < 0.0001$ ; **Figure 1C**). High-throughput next-generation sequencing was then conducted  
60 on extracted mRNA from BLA and target areas. Counts of unique barcodes from the extracted  
61 RNA were normalized and a threshold applied to control for spurious sequencing results<sup>7</sup>  
62 (Extended Data Figure 2). The combined thresholded barcode counts from the four  
63 hemispheres were then analyzed together (see Extended Data Figures 3 and 4 for analyses of  
64 each hemisphere separately and comparisons between hemispheres, respectively).

65 In total, we recovered 3,115 unique barcodes in samples dissected from BLA across the  
66 four hemispheres. This yield of barcode counts is similar in level to that recovered in mice per  
67 injection<sup>21-24</sup>, indicating that MAPseq<sup>7</sup> was working as intended in macaques. To determine the  
68 projection targets of putative single neurons from BLA, we then determined whether each  
69 barcode found in amygdala was present in any of the target areas after collapsing across all  
70 samples in a target area. Approximately one-third of the unique barcodes – which can be  
71 interpreted to represent single neurons – projected only to other sites within amygdala, which  
72 we refer to as zero-target. Another third projected to only one of the target areas we collected  
73 – we refer to these neurons as having *specific* projections – and the remaining third had two or  
74 more targets outside of amygdala. We refer to these neurons with multiple targets as having  
75 *branching* projections (**Figure 1D**).

76 The overall proportion of barcode recovered in each target mirrored known connections  
77 of BLA in macaques (**Figure 1E**). Accordingly, the highest amount of barcode was recovered in  
78 entorhinal cortex and nucleus accumbens (NAcc), two areas which have previously been  
79 identified as receiving dense projections from BLA<sup>25</sup>. A lower amount of barcode was recovered  
80 from hippocampus and agranular insula (AI), which are also well-documented as receiving  
81 strong projections from BLA<sup>4,26</sup>, followed by subcallosal (scACC) and dorsal ACC (dACC).  
82 Notably, relatively similar amounts of barcode were recovered from all other target areas in  
83 frontal cortex and striatum, which again matches known gradients of BLA connections across  
84 the frontal lobe<sup>4,27</sup>. The close alignment between our findings and prior tract-tracing supports  
85 the validity of MAPseq in quantifying coarse area-to-area projections in macaques.

86           Next, we looked at the probability that a barcode found in one target structure was also  
87 found in another target structure (**Figure 1F**). This approach allowed us to begin to ascertain  
88 the degree to which connections of single BLA neurons are either specific or branching. For  
89 instance, neurons that project to NAcc have a high probability of also projecting to AI. By  
90 contrast, single neurons that project to AI are unlikely to project to either entorhinal cortex or  
91 hippocampus. Similar patterns of non-overlapping projections are also apparent in BLA  
92 projections to frontal cortex; neurons that project to medial orbitofrontal cortex (mOFC) are  
93 unlikely to project to ventrolateral prefrontal cortex (vlPFC). As can be seen in by the  
94 representative examples in **Figure 1G**, evidence for both specific and branching projection  
95 patterns can be observed at the level of single neurons, as well. Notably, our results correspond  
96 closely with the findings of two studies that investigated the patterns of BLA neuron branching  
97 to frontal cortex and thalamus. One by Sharma, Fudge and colleagues<sup>28</sup> identified a subset of  
98 amygdala neurons that project to adjacent parts of medial frontal areas 25/14 (which we refer  
99 to as scACC and mOFC, respectively) and 32/24 (which encompasses our perigenual ACC  
100 [pgACC] and dACC, respectively). We also identified neurons that projected to both areas,  
101 although we identified a slightly higher proportion of neurons with this branching pattern  
102 (between 7 and 20% depending on the animal) of them than previously reported (between 7  
103 and 10% depending on the nucleus) – likely because our dissected areas encompassed larger  
104 portions of medial frontal cortex. A study by Timbie and Barbas<sup>29</sup> found that two largely non-  
105 overlapping populations of amygdala neurons projected to either MD or posterior OFC/AI, a  
106 result highly similar to what we found (**Figure 1F**). This lack of branching as discerned by our  
107 barcode analysis is an important negative finding; in addition to observing the expected  
108 pattern of *branching projections* to certain targets, we have also observed the expected pattern  
109 of *specific projections* to other targets. Taken together the above analyses provide novel  
110 evidence that BLA neurons often project to multiple targets in frontal cortex, arguing against  
111 specific targeting as the dominant connectivity principle, while also reproducing the known  
112 gross connectivity of BLA – altogether confirming the validity of MAPseq in macaques.

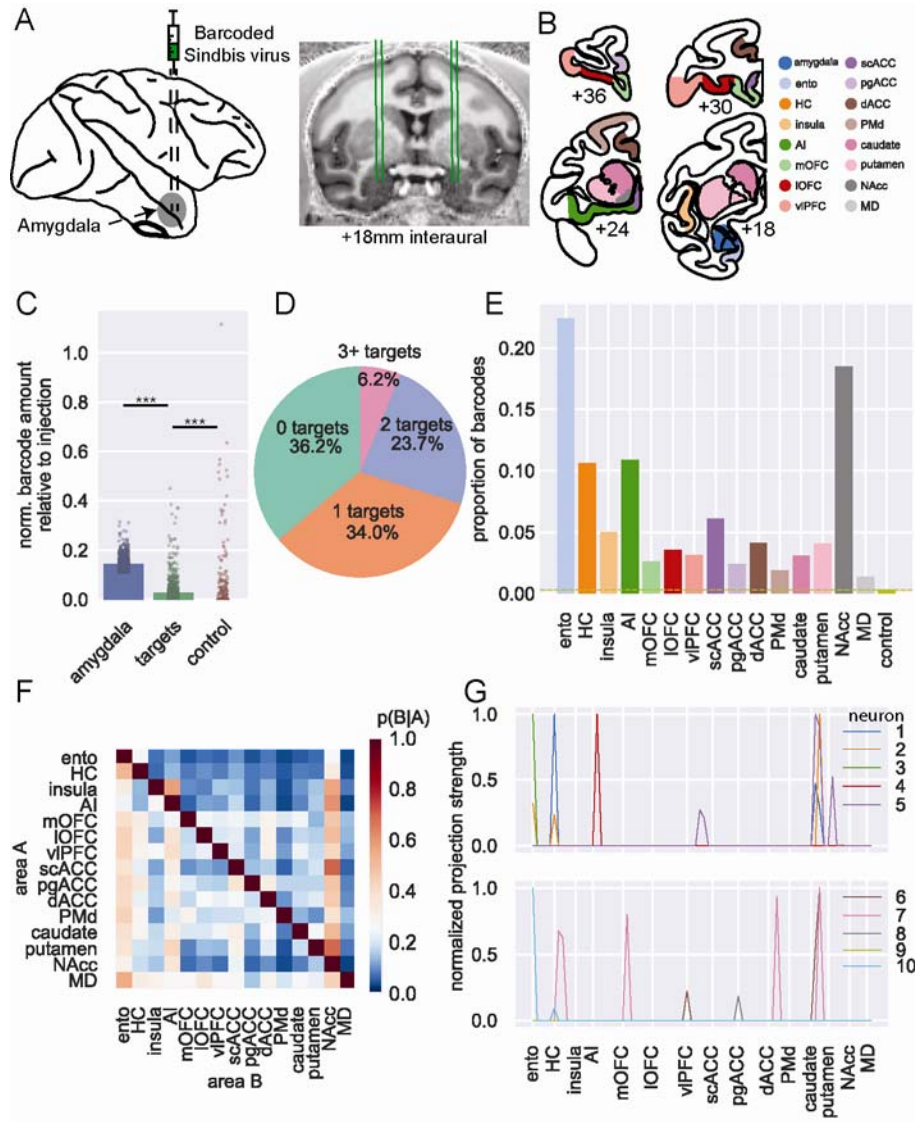


**Figure 1: MAPseq of macaque BLA.** **A)** Schematic of injection approach. **B)** Example coronal sections showing dissection targets in striatum as well as frontal and temporal lobes. Ento, entorhinal; HC, hippocampus (not shown); AI, anterior insula cortex; mOFC, medial orbitofrontal cortex; IOFC, lateral orbitofrontal cortex; vlPFC, ventrolateral prefrontal cortex; scACC, subcallosal anterior cingulate cortex; pgACC, perigenual ACC; dACC, dorsal ACC; PMd, dorsal premotor cortex; NAcc, nucleus accumbens; MD, mediodorsal thalamus (also not shown). Anterior-posterior levels are in mm relative to the interaural plane. **C)** Normalized barcode amount relative to peak barcode amount in injection site across other locations in amygdala (blue), all target structures (green; OLS regression vs amygdala:  $t(2) = 46.43, p < 0.0001$ ), and control areas (red; vs targets:  $t(2) = 4.77, p < 0.001$ ). **D)** Proportion of unique barcodes in no targets outside of amygdala (green), one (orange), two (blue), or more than two targets outside of amygdala (red). **E)** Proportion of barcodes in each of the target and control areas; dashed line indicates the proportion of barcode found in control sites. **F)** Conditional probability that a barcode in area A is also found in area B. Note that the order of indexing here alters the probability such that  $P(A|B)$  can be greater than  $P(B|A)$ . **G)** Normalized proportion of barcodes across all the potential target areas and control areas for 10 unique barcodes (colored lines).



## 114 Quantitative analysis of branching connective motifs of single BLA neurons

115 The prior analysis on the branching of neurons to two targets, while revealing, does not  
116 capture the full set of connections that single neurons make to multiple target areas – one of  
117 the major strengths of MAPseq over standard tract-tracing approaches (**Figure 1G**).  
118 Consequently, we focused our next analysis on the nearly 1,300 BLA neurons with branching  
119 projections to multiple locations in frontal cortex, temporal cortex, striatum and thalamus  
120 (**Figure 2A**). While all target areas received the majority of their input from branching neurons,  
121 entorhinal cortex was found to receive the highest proportion of specific input from BLA (**Figure**  
122 **2B**, z-test for proportions: entorhinal vs hippocampus [next highest],  $z = 10.67$ ,  $p < 0.0001$ ).  
123 Next, to determine whether any branching motifs were over- or under-represented compared  
124 to chance, we built a null distribution based on the overall barcode distribution (**Figure 2C**).  
125 Assuming total independence for branching, the probability that a neuron projects to both  
126 areas A and B can be computed as the product of the independent probabilities of projecting to  
127 area A and area B<sup>24</sup>. By comparing the actual counts for each motif with this null distribution,  
128 we identified only one over-represented bifurcating motif: neurons that project to both NAcc  
129 and AI (binomial test,  $p = 0.003$ ). This motif was found alongside predominantly under-  
130 represented bi- and trifurcations, many of which included projection motifs encompassing  
131 some combination of NAcc, entorhinal cortex, and hippocampus (**Figure 2D and 2E**). That  
132 branching to only two of these areas happens less frequently than expected is somewhat  
133 surprising considering these were the three areas most likely to receive projections from BLA in  
134 our data (**Figure 1E**); however, these data are in line with small-world theories of brain network  
135 organization<sup>30</sup>. By contrast, axon branching to four different targets were far more likely to be  
136 over-represented compared to that same chance distribution (**Figure 2F**). In other words, there  
137 are fewer bifurcations than expected based solely on the proportions of barcodes found in each  
138 target area, while there were more of these quadfurcations than expected. There were no  
139 significantly over- or under-represented motifs with five or more targets. Thus, these results  
140 indicate that single BLA neurons demonstrate a high degree of branching, being more likely to  
141 strongly innervate four distinct targets in the target areas sampled over two or three.  
142 Importantly, this analysis also reveals that the observed branching motifs are not simply a

143 product of the distribution of barcodes; rather, branching of single BLA neurons appears to be  
 144 highly structured.

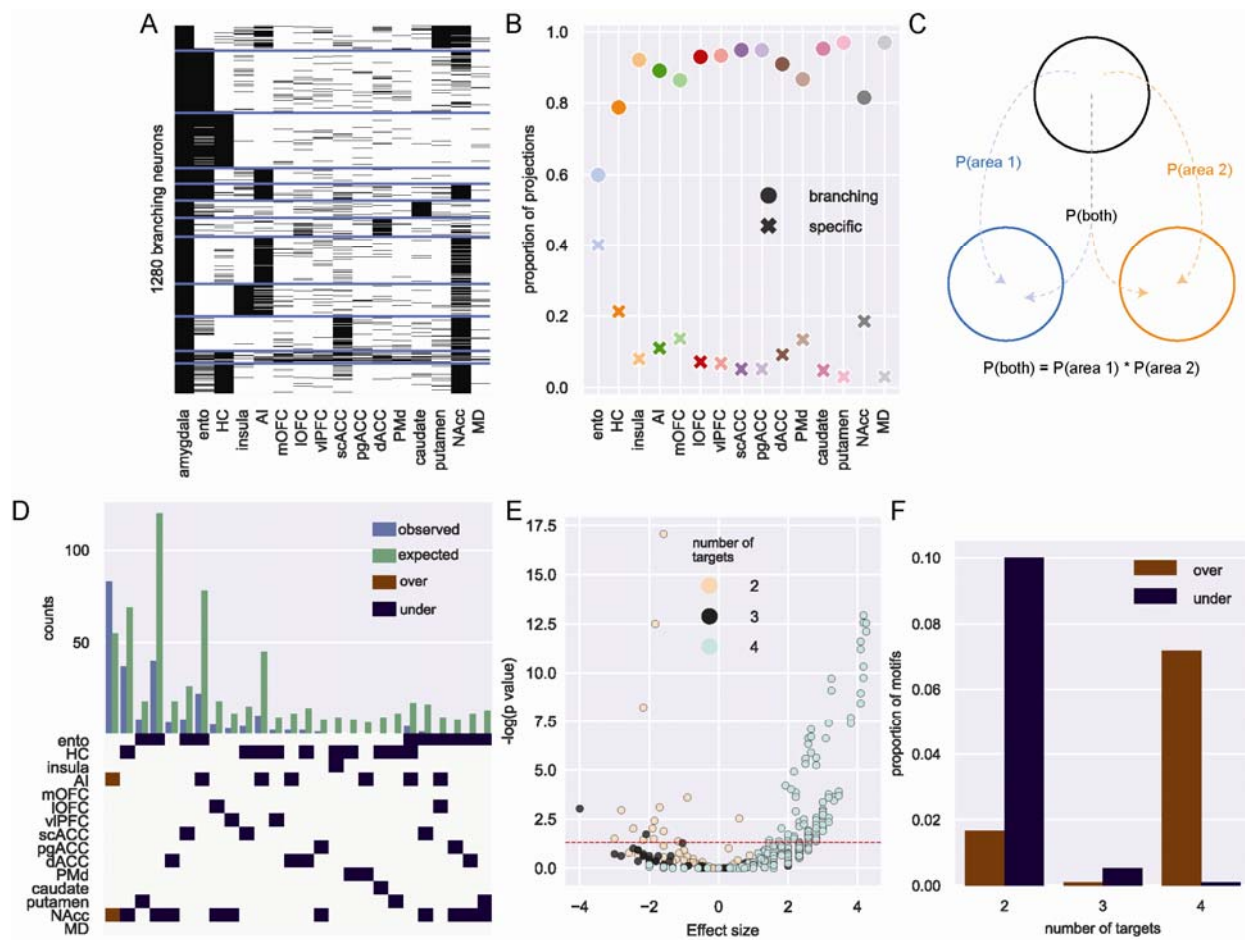


**Figure 2: Single neuron analysis of branching projections from BLA.** **A**) K-means clustering of 1,300 neurons that project to more than one area outside of amygdala (k=12). **B**) Proportion of projections from BLA to frontal cortex areas, striatum, and mediodorsal thalamus that are from specific (crosses) or branching projections (filled circles). **C**) Logic of null distribution computation for branching motifs. **D**) Observed (blue) and expected (green) counts of neurons with projections to multiple areas (top). Specific over (red) or under-represented (blue) branching motifs by area (bottom). **E**) Volcano plot of probability of all possible branching motifs with 2 (cream), 3 (grey), and 4 (turquoise) target areas. Dashed line marks the level of statistical significance. **F**) Proportion of significantly over- (red) and under- (blue) represented 2-, 3- and 4- target area branching motifs.

## 145 Single neuron projection networks within frontal cortex

146 With the appreciation that the projections of single neurons in BLA are highly likely to  
 147 branch to multiple areas we sought to understand how these projections are organized. Here  
 148 we separately focused on the patterns of single BLA projections to the medial and ventral frontal  
 149 cortex. We took this approach because BLA projections to these areas are thought to be  
 150 functionally distinct. Interaction between BLA and medial frontal cortex is heavily linked to

151 defensive threat conditioning in animals and anxiety-related disorders such as PTSD in  
152 humans<sup>31</sup>. Projections from BLA to ventral frontal cortex are, by contrast, more frequently  
153 associated with reward-guided behaviors<sup>6</sup> and dysfunction in these circuits is linked to addictive  
154 disorders<sup>32</sup>.

#### 155 *Medial frontal cortex*

156 We identified 405 BLA neurons that project to either medial frontal areas scACC (area  
157 25 as defined by Carmichael and Price<sup>33</sup>), pgACC (area 32), or dACC (area 24) (**Figure 3A**).  
158 Although these areas are densely interconnected<sup>18</sup>, we found marked differences in the  
159 structure of BLA input that they receive. First, over half of the BLA neurons that projected to  
160 medial frontal cortex exclusively targeted scACC, whereas a third targeted only dACC (130/405;  
161 z-test for proportions,  $z = 6.38$ ,  $p < 0.0001$ ); even fewer BLA projections to medial frontal cortex  
162 were specific to pgACC (55/405;  $z = 6.28$ ,  $p < 0.0001$ ) (**Figure 3B**). Indeed, the majority of BLA  
163 neurons targeting pgACC also projected to the other parts of medial frontal cortex, while a  
164 smaller proportion of dACC-projecting neurons branched within medial frontal cortex ( $z = 5.37$ ,  
165  $p < 0.0001$ ); scACC-projecting neurons were least likely to branch ( $z = 3.17$ ,  $p = 0.0015$ ). Thus,  
166 within medial frontal cortex there is a hierarchy of specific vs branching BLA connections where  
167 pgACC receives the least specific BLA input and scACC receives the most.

168 As we noted earlier, BLA neurons tend to have more branching than specific projections  
169 (**Figure 2C and E**); within this branching, we found additional structure among projections that  
170 targeted single medial frontal areas. Neurons that project to scACC or dACC were more likely to  
171 have four targets than neurons which projected to pgACC, which were dominated by two- and  
172 three- target neurons (**Figure 3C**, permutation test). These results suggest that amygdala inputs  
173 to pgACC, while frequently shared among other cingulate areas, are not shared as frequently  
174 outside of medial frontal cortex.

175 Within the projections from BLA to medial frontal cortex there were notable differences  
176 in the areas that these single neurons also targeted, indicative of different networks. Whereas  
177 the BLA neurons projecting to each medial area had similar proportions of bifurcations to  
178 hippocampus and entorhinal cortex (**Figure 3D and E**), neurons that projected to scACC were far  
179 more likely to also project to NAcc than the other areas (z-test for proportions: scACC vs pgACC:

180  $z = 5.85, p < 0.0001$ ; scACC vs dACC:  $z = 6.33, p < 0.0001$ ). This projection motif is evident at the  
181 level of individual neurons, and these cells were also highly likely to connect to AI (**Figure 3E**).  
182 dACC-projecting BLA neurons, however, were more likely to also project to lateral OFC (lOFC;  
183 dACC vs pgACC:  $z = 2.72, p = 0.0097$ ; dACC vs scACC:  $z = 3.80, p < 0.001$ ) and vIPFC (dACC vs  
184 pgACC:  $z = 2.04, p = 0.061$ ; dACC vs scACC:  $z = 3.52, p < 0.001$ ) on the ventral surface of the  
185 frontal lobe, providing further anatomical support for the role of the dACC in valuation through  
186 its interactions with more ventral areas<sup>6,34</sup>. In summary, single BLA neurons targeting medial  
187 frontal areas appeared to target distinct networks; those targeting scACC were largely  
188 constrained to this area and primarily sent bifurcations to NAcc and AI in the posterior ventral  
189 frontal cortex, consistent with the known roles of these areas in regulating mood<sup>35</sup>. By contrast,  
190 those targeting dACC also innervated parts of ventral frontal cortex including those linked to  
191 Carmichael and Price's visceromotor network<sup>18</sup>, consistent with its role in value-based decision-  
192 making<sup>6,34</sup>.

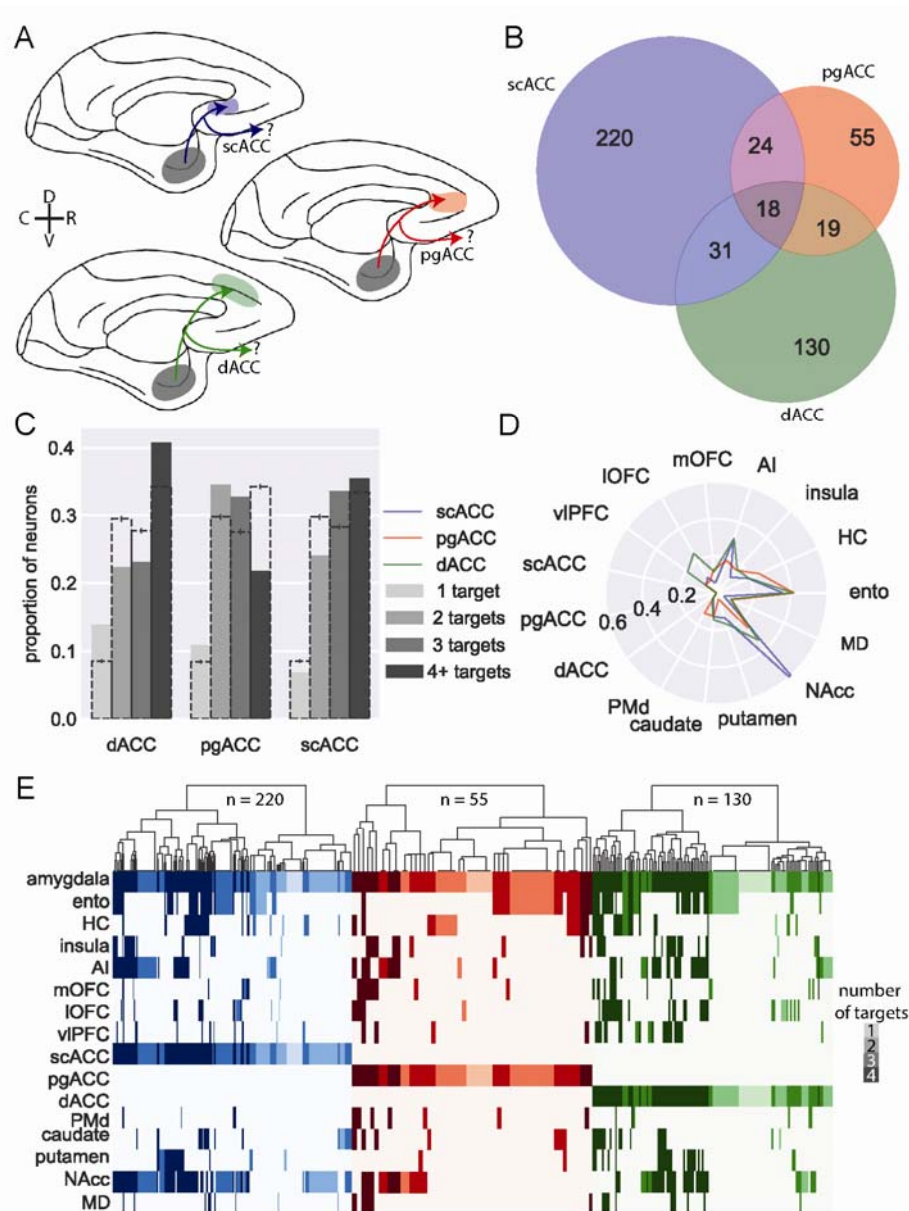


**Figure 3: BLA specific projections to medial frontal cortex.** **A)** Schematic showing the three populations of medial frontal cortex-projecting neurons analyzed here: BLA neurons targeting scACC (blue), pgACC (red), dACC (green). **D** and **V** refer to the dorsal and ventral directions, respectively; **R** and **C** designate rostral and caudal. **B)** Venn diagram illustrating projections to each medial frontal cortex area that also branch to the other two; pgACC-projecting neurons are more likely to branch than dACC-projecting neurons (z-test for proportions,  $z=3.17$ ,  $p=0.0015$ ), which are more likely to branch than scACC-projecting neurons ( $z=2.27$ ,  $p=0.023$ ). **C)** Degrees of branching for each medial frontal cortex-projecting population; dashed bars indicate the mean of 1000 shuffles of the data, downsampled for equal numbers of neurons from each population; error bars indicate 95% confidence intervals. **D)** Likelihood of medial frontal cortex-projecting neurons projecting to non-medial frontal cortex targets. **E)** Single-neuron projection patterns; shading indicates number of targets.

194           **Ventral Frontal Cortex Networks**

195           We conducted a similar analysis on the 627 BLA neurons that projected to areas on the  
196 ventral surface of frontal cortex, including AI, mOFC, IOFC, and vIPFC (**Figure 4A**). Of those BLA  
197 neurons that projected to ventral frontal cortex, almost two thirds (65%) of BLA neurons solely  
198 targeted AI, whereas only 10% solely targeted vIPFC; within ventral frontal cortex, these areas  
199 received the highest and lowest proportions of specific projections, respectively (z-test for  
200 proportions:  $z = 19.85$ ,  $p < 0.0001$ , **Figure 4B**). Indeed, the majority of BLA neurons projecting to  
201 vIPFC also targeted other parts of the ventral frontal cortex and were not specific to this area.  
202 BLA neurons projecting to mOFC and IOFC had similar proportions of cells projecting in a  
203 specific or branching manner. Thus, BLA projections to AI are more specific compared to those  
204 directed to more anterior regions (AI vs mOFC:  $z = 4.43$ ,  $p < 0.0001$ ), with vIPFC receiving the  
205 fewest specific projections from BLA (vIPFC vs mOFC:  $z = 2.48$ ,  $p = 0.013$ ).

206           Similar to medial frontal cortex, BLA neurons projecting to ventral frontal cortex were  
207 more likely to send branching as opposed to specific projections. AI-, IOFC-, and vIPFC-  
208 projecting neurons were most likely to send 2-target projections (**Figure 4C**, permutation test),  
209 whereas mOFC-projecting neurons tended to innervate either one or four targets. AI- and  
210 vIPFC-projecting neurons were least likely to branch to four distinct targets, suggesting that  
211 these two areas receive the most highly specialized input from BLA.

212           When we limited our analyses to BLA neurons that only projected to one of the four  
213 ventral frontal areas without branching between them, BLA neurons that project to AI exhibited  
214 the strongest projections to NAcc compared to other areas in ventral frontal cortex (**Figure 4C**  
215 and **E**; Fisher's exact test: AI vs mOFC,  $p = 0.0057$ ; AI vs IOFC,  $p = 0.00019$ ; AI vs vIPFC,  $p <$   
216  $0.0001$ ). By contrast, vIPFC- and IOFC- projecting neurons were most likely to also project to  
217 entorhinal cortex compared to mOFC and AI (**Figure 4C**; IOFC vs mOFC,  $p = 0.043$ ; IOFC vs AI,  $p <$   
218  $0.0001$ ; vIPFC vs AI,  $p = 0.00051$ ). Somewhat unexpectedly, BLA neurons with projections to  
219 mOFC were more likely to project to dorsal premotor cortex (PMd; mOFC vs AI,  $p < 0.00001$ ;  
220 mOFC vs IOFC,  $p = 0.028$ ) and other more medial areas of the frontal lobe such as the pgACC  
221 (**Figure 4C and E**; mOFC vs AI,  $p = 0.019$ ; mOFC vs IOFC,  $p = 0.038$ ) than were BLA neurons  
222 projecting to other ventral frontal cortex regions. These patterns of projections indicate the BLA

223 neurons targeting the ventral frontal cortex form highly-structured networks; those targeting AI  
224 are less likely also to project to other ventral frontal areas. When they do branch to other areas,  
225 they primarily innervate other areas in the posterior frontal lobe (i.e. scACC) and NAcc. By  
226 contrast, BLA projections to more anterior parts of ventral frontal cortex, especially vIPFC,  
227 branch more both within frontal cortex and also to other areas. This finding that vIPFC-  
228 projecting neurons connect so broadly aligns closely with the known role of the BLA-vIPFC  
229 circuit in representing and updating model-free stimulus-outcome associations<sup>36</sup>, information  
230 that is likely to be shared among other ventral frontal areas to inform reward-guided choice  
231 behavior<sup>37</sup>.

232         Taken together, the patterns of projections strongly indicate the existence of BLA  
233 neurons that target distinct networks in the medial and ventral frontal cortex. Those BLA  
234 neurons that target scACC and AI in the posterior frontal cortex preferentially innervate NAcc.  
235 By contrast, BLA neurons that target to more anterior medial and ventral frontal areas appear  
236 to be part of more distributed networks of areas. This extends our understanding of the  
237 organization of BLA-to-frontal cortex networks revealing distinct connective motifs that may  
238 in part explain the pervasive influence of BLA on frontal cortex processing.

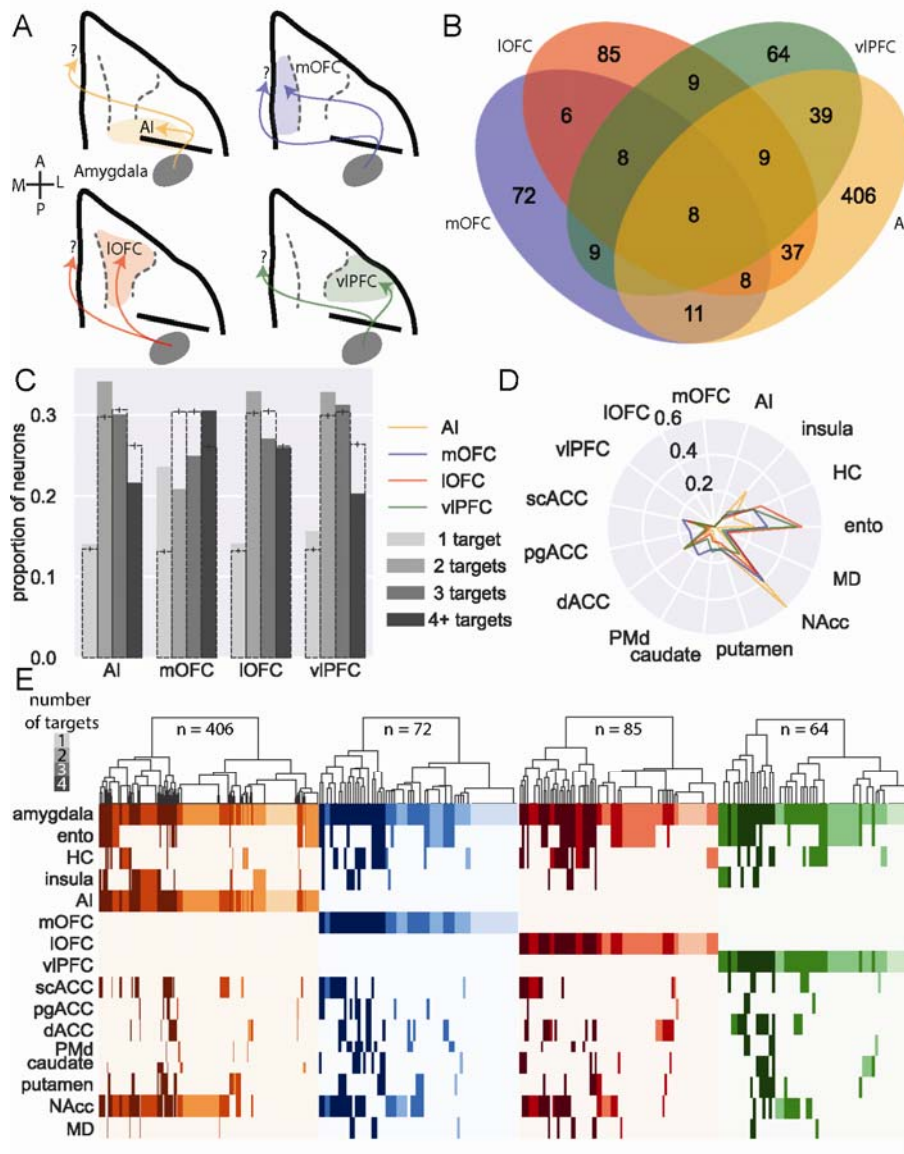


**Figure 4: BLA specific projections to ventral frontal cortex.** **A)** Schematic showing the four populations of ventral frontal cortex-projecting neurons analyzed here: BLA neurons targeting AI (yellow), mOFC (blue), IOFC (red), and vIPFC (green). A and P designate anterior and posterior directions, respectively; M and L refer to medial and lateral. **B)** Venn diagram illustrating projections to each area that also branch to the other three; AI-projecting neurons were least likely to branch to the other areas (z-test for proportions,  $z=4.425$ ,  $p<0.0001$ ), while vIPFC-projecting neurons were most likely to branch within ventral FC ( $z=2.476$ ,  $p=0.0133$ ). **C)** Degrees of branching for each ventral frontal cortex-projecting population; dashed bars indicate the mean of 1000 shuffles of the data, downsampled for equal numbers of neurons from each population; error bars indicate 95% confidence intervals. **D)** Likelihood of ventral frontal cortex-projecting neurons projecting to non-ventral frontal cortex targets. **E)** Single-neuron projection patterns; shading indicates number of targets.



240 **Retrograde tracing validation of specific and branching BLA projections to ventral frontal**  
241 **cortex**

242         Next, we sought to assess the most distinct BLA projection patterns revealed by MAPseq  
243 using standard retrograde viral tracing. In a single macaque, MRI-guided stereotactic injections  
244 of retro-AAV2 coding for mCherry and EGFP fluorophores were injected into NAcc and a lateral  
245 subregion of AI in one hemisphere. Injections were targeted to posterior-lateral IOFC (area 13m  
246 as defined by Carmichael and Price<sup>33</sup>) and posterior-medial vIPFC (area 12o) in the other  
247 hemisphere (**Extended Data Figure 5A and B**). As cross-hemispheric BLA connections are  
248 negligible<sup>27</sup>, we were able to analyze the two hemispheres separately. We then conducted  
249 unbiased stereological counting of neurons in BLA that were either single or double labeled  
250 with each fluorophore in each hemisphere<sup>38</sup>. Thus, we were able to compare the connectivity  
251 profiles of single amygdala neurons found in specific subregions of frontal cortex.

252         For BLA neurons projecting to AI, we found a high degree of correspondence in the  
253 proportion of branching neurons between stereology and MAPseq estimates (z-test for  
254 proportions  $p > 0.05$ , Extended Data Figure 5C); for NAcc-projecting neurons, however, our  
255 MAPseq and stereology results did not agree, as stereological estimates of specific projections  
256 were higher than MAPseq ( $p < 0.0001$ ). For IOFC and vIPFC, too, the numbers of BLA neurons  
257 that projected specifically to one or branched to both areas was different to what we found  
258 with MAPseq ( $p < 0.001$ , Extended Data Figure 5D). This was primarily because stereological  
259 estimates of BLA projections to vIPFC almost entirely overlapped with those targeting IOFC. The  
260 difference in estimates of specific versus branching BLA projections between retrograde tracing  
261 and MAPseq results is not unexpected<sup>22</sup>. This is because the injections of retro-AAV into IOFC  
262 and vIPFC do not cover the full extent of these cortical regions. By contrast, MAPseq estimates  
263 of specific and branching projections are based on BLA projections to the whole of IOFC and  
264 vIPFC that extend far beyond the extent of the areas target with retro-AAV. The difference in  
265 estimates of the branching and specific projections between techniques is, however, revealing  
266 as it indicates that projections to this subregion of area 12 are even less specific than the  
267 analysis of connectivity of the larger vIPFC would indicate.

268 **Branching and specific projections shape fMRI functional connectivity**

269 Anatomical connections in the brain constrain functional networks<sup>39,40</sup>. Given the  
270 reproducible patterns of specific and branching projections from BLA that we identified, we  
271 sought to determine if multi-area connectional motifs identified by MAPseq could be identified  
272 at the level of fMRI functional connectivity (FC). If such patterns were identifiable in FC this  
273 would indicate that the unique anatomical networks identified with MAPseq are related to and  
274 in fact shape functional networks in the brain. We analyzed a dataset of resting state fMRI  
275 scans from six rhesus monkeys<sup>41</sup> (**Figure 5A**), with single seed voxels in amygdala and target  
276 voxels in the same areas used in the MAPseq experiments (Extended Data Figure 6). After  
277 computing and z-transforming FC values for each amygdala voxel with each target voxel, we  
278 binarized the FC signal by setting a threshold at 70% of each voxels' maximum connectivity.  
279 Practically, this meant that if FC between an amygdala voxel and any target area was above the  
280 threshold, we counted that amygdala voxel as being *functionally connected* to that target area.  
281 We then counted the number of connections to each target area and normalized those counts  
282 by the size of each target area. This approach meant that single amygdala voxels could be  
283 designated as being functionally connected to multiple parts of frontal cortex, striatum,  
284 temporal lobe and thalamus, following a similar approach to MAPseq.

285 Despite fMRI-derived FC operating over a much larger spatial scale than standard  
286 anatomical approaches and having no directional sensitivity, we were still able to identify a  
287 largely similar pattern of relative FC between amygdala and our target areas as we had found  
288 with MAPseq (compare **Figures 1E** and **5C**). Notably, the pattern also generally matches prior  
289 tract-tracing results as there was strong connectivity between amygdala and entorhinal cortex,  
290 hippocampus, NAcc, AI, scACC as well as MD with lower connectivity to IOFC and pgACC<sup>42</sup>. For a  
291 number of areas, functional connectivity with amygdala was higher than expected based on  
292 MAPseq and tract-tracing data, most notably PMd and mOFC (**Figure 5C**). This result is not  
293 necessarily surprising because FC measures not only reflect unidirectional connections from  
294 one area to another; rather, strong functional connection between two areas can be driven by  
295 strong reciprocal connections or strong coupling with a third area with which both areas  
296 strongly interact<sup>43</sup>.

297           Next to look for patterns of network-level connectivity we assessed the FC of amygdala  
298 voxels with high connectivity to areas in medial frontal cortex (**Fig. 5C**) or ventral frontal cortex  
299 (**Fig. 5D**). This is essentially the same analysis depicted in **Figures 3E** and **4E**. Notably, we were  
300 able to identify many of the prominent connectivity motifs that we observed with MAPseq. For  
301 instance, voxels with a high likelihood of being connected to AI neurons also had higher  
302 connectivity with NAcc (**Figure 5D**). Similarly, dACC-connected neurons also had a high  
303 likelihood of being connected to vIPFC (**Figure 5C**) and if a voxel showed high FC with any of the  
304 medial and ventral frontal cortex areas it had uniformly low connectivity with MD (**Figures 5C**  
305 **and D**). This latter point demonstrates the correspondence between MAPseq, tract-tracing and  
306 fMRI<sup>42</sup>.

307           Despite being able to discern these broad connectional motifs, some key differences  
308 between medial and ventral areas were obscured, such that fMRI estimates of multi-region  
309 connectivity estimated highly similar connectivity profiles for all three medial frontal cortex  
310 areas. This difference between fMRI and MAPseq analyses is likely explained by the dense and  
311 bidirectional interconnections within medial frontal cortex<sup>18</sup>, inputs from other structures  
312 received by this part of frontal cortex most notably from hippocampus and neuromodulatory  
313 systems<sup>27,44</sup>, and the low resolution of fMRI compared to individual neurons. Taken together,  
314 that major anatomical features identified by MAPseq were also identifiable at the level of fMRI  
315 FC likely reflects their significance in shaping brain-wide activity patterns organized into  
316 functional networks.

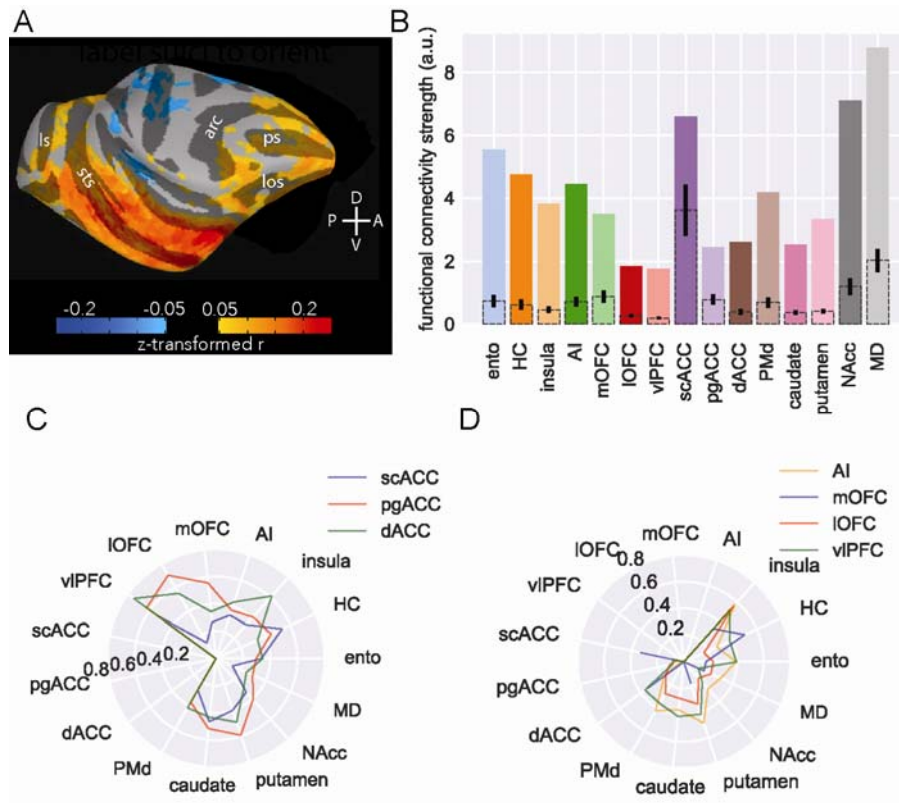


**Figure 5: MRI functional connectivity replicates some anatomical features.** A) Surface projection of right amygdala ROI functional connectivity to right hemisphere targets, averaged across six animals. Compass directions refer to dorsal (D)/ventral (V) and posterior (P)/anterior (A) directions; sulci labelled are: principal sulcus (ps), lateral orbital sulcus (los), arcuate sulcus (arc), superior temporal sulcus (sts), lunate sulcus (ls). B) Functional connectivity strength across areas. Colored bars indicate number of amygdala voxels functionally connected to each target area, corrected for the number of voxels in each target area; dotted bars with 95% confidence intervals indicate random samples of the same number of voxels from each area as the smallest target area (scACC). C) Likelihood of medial FC-projecting voxels being functionally connected to non-medial FC targets. D) Likelihood of ventral FC-projecting voxels being functionally connected to non-ventral FC targets.

317

## 318 Discussion

319 We have optimized and validated MAPseq for single-neuron connectivity mapping in  
 320 macaque monkeys, opening new avenues of research into the single-cell structural connections  
 321 of the non-human primate brain. Using this approach, we successfully determined the  
 322 projection patterns of over 3,000 single neurons from BLA to frontal cortex, striatum, parts of  
 323 the temporal lobe, and MD. Notably, the bulk patterns of connections identified here are in  
 324 close alignment with previous reports of BLA projections based on traditional tract-tracing

325 techniques<sup>45,1,2,25,3,26,29</sup> (**Figures 1 and 2**). Overall, we found that single BLA neurons branch  
326 extensively, with branching to four distinct targets being more likely to be over-represented  
327 compared to chance than branching to two or three targets (**Figure 2**). Within these patterns of  
328 branching, we identified distinct connectional motifs; BLA projections to posterior parts of the  
329 medial and ventral frontal cortex were highly specific and less likely to branch to other areas. By  
330 contrast, projections to more anterior or dorsal areas were much more likely to branch to other  
331 brain areas and exhibited unique projection profiles (**Figures 3 and 4**). We also identified broad  
332 similarities and slight differences between this anatomical connectivity and more standard  
333 tract-tracing techniques (**Extended Data Figure 5**) and functional connectivity identified by fMRI  
334 (**Figure 5**). These findings begin to reveal the unique patterns of projections of single BLA  
335 neurons, connections that are heavily implicated in the control of affect and that become  
336 dysfunctional in psychiatric disorders<sup>11</sup>.

337         It is well documented that BLA input to frontal cortex is strongest to posterior regions  
338 and weaker to more anterior regions<sup>2,4</sup>. On top of this, we found that in both medial and  
339 ventral frontal cortex, BLA neuron branching is highest to the most anterior areas. For instance,  
340 BLA neurons projecting to pgACC showed the highest degree of branching to other areas in  
341 medial frontal cortex, whereas neurons projecting to the more posterior scACC branched the  
342 least (**Figure 3B**). A generally similar pattern was seen in ventral frontal cortex with the  
343 exception of vlPFC, which received the highest degree of branching projections (**Figure 4**). This  
344 lack of specific BLA projections to vlPFC may be related to its role in model-free as opposed to  
345 model-based behaviors; lesions of vlPFC do not impact reinforcer devaluation that depends on  
346 specific sensory information about an outcome but do impact outcome-independent  
347 probabilistic learning<sup>36</sup>. Thus, the patterns of specific and branching connections from single  
348 BLA neurons may serve a functional role in relaying distinct sensory information or providing a  
349 salience signal to invigorate responding, respectively. In medial frontal cortex, while so-called  
350 ventromedial PFC has been generally implicated in affective regulation, and by extension  
351 anxiety and mood disorders<sup>46</sup>, more recent evidence suggests that particular subregions may  
352 play distinct roles in affect<sup>47-49</sup>. The highly specific and segregated inputs to scACC and pgACC

353 identified here potentially provide a neuroanatomical basis for their opposing roles in affective  
354 responding<sup>35</sup>.

355         Appreciating the unique features of BLA projections to frontal cortex is potentially  
356 critical for understanding the basis of a number of amygdala-linked psychiatric disorders<sup>11</sup>. For  
357 example, obsessive-compulsive disorder is associated with dysfunction in basal ganglia-OFC  
358 circuitry regulating valuation as well as basal ganglia-dACC circuits involved in action selection<sup>50</sup>.  
359 Here we identified a population of dACC-projecting BLA neurons that also preferentially  
360 targeted parts of ventral frontal cortex including IOFC (**Figure 3**). Our findings therefore provide  
361 a potential anatomical basis through which dysfunction in a single, small population of BLA  
362 neurons could influence a distributed network of areas. Determining the distinct functions of  
363 the different BLA projection motifs identified here as well as their molecular signatures<sup>23,51</sup> has  
364 the potential to bring network-level understanding to basic and translational neuroscience and  
365 might provide a more biologically-realistic basis for the construction of neural network  
366 architectures<sup>52</sup>.

## 367 References

- 368 1. Aggleton, J. P. & Mishkin, M. Projections of the amygdala to the thalamus in the  
369 cynomolgus monkey. *J. Comp. Neurol.* **222**, 56–68 (1984).
- 370 2. Amaral, D. G. & Price, J. L. Amygdalo-cortical projections in the monkey (Macaca  
371 fascicularis). *Journal of Comparative Neurology* **230**, 465–496 (1984).
- 372 3. Ghashghaei, H. T. & Barbas, H. Pathways for emotion: interactions of prefrontal and  
373 anterior temporal pathways in the amygdala of the rhesus monkey. *Neuroscience* **115**,  
374 1261–1279 (2002).
- 375 4. Ghashghaei, H. T., Hilgetag, C. C. & Barbas, H. Sequence of information processing for  
376 emotions based on the anatomic dialogue between prefrontal cortex and amygdala.  
377 *NeuroImage* **34**, 905–923 (2007).
- 378 5. Bucy, P. C. & Klüver, H. An anatomical investigation of the temporal lobe in the monkey  
379 (Macaca mulatta). *Journal of Comparative Neurology* **103**, 151–251 (1955).
- 380 6. Rudebeck, P. H., Ripple, J. A., Mitz, A. R., Averbeck, B. B. & Murray, E. A. Amygdala  
381 Contributions to Stimulus–Reward Encoding in the Macaque Medial and Orbital Frontal  
382 Cortex during Learning. *J. Neurosci.* **37**, 2186–2202 (2017).
- 383 7. Kebuschull, J. M. *et al.* High-Throughput Mapping of Single-Neuron Projections by  
384 Sequencing of Barcoded RNA. *Neuron* **91**, 975–987 (2016).
- 385 8. Davis, M. & Whalen, P. J. The amygdala: vigilance and emotion. *Mol Psychiatry* **6**, 13–34  
386 (2001).
- 387 9. Horvath, F. E. Effects of basolateral amygdectomy on three types of avoidance behavior in  
388 cats. *Journal of Comparative and Physiological Psychology* **56**, 380–389 (1963).
- 389 10. Sengupta, A. *et al.* Basolateral Amygdala Neurons Maintain Aversive Emotional Salience. *J.*  
390 *Neurosci.* **38**, 3001–3012 (2018).
- 391 11. Schumann, C. M., Bauman, M. D. & Amaral, D. G. Abnormal structure or function of the  
392 amygdala is a common component of neurodevelopmental disorders. *Neuropsychologia* **49**,  
393 745–759 (2011).
- 394 12. Brady, R. O. *et al.* State dependent cortico-amygdala circuit dysfunction in bipolar disorder.  
395 *Journal of Affective Disorders* **201**, 79–87 (2016).

- 396 13. Marusak, H. A. *et al.* You say ‘prefrontal cortex’ and I say ‘anterior cingulate’: meta-analysis  
397 of spatial overlap in amygdala-to-prefrontal connectivity and internalizing symptomology.  
398 *Transl Psychiatry* **6**, e944–e944 (2016).
- 399 14. Yin, S., Liu, Y., Petro, N. M., Keil, A. & Ding, M. Amygdala Adaptation and Temporal  
400 Dynamics of the Salience Network in Conditioned Fear: A Single-Trial fMRI Study. *eNeuro* **5**,  
401 (2018).
- 402 15. Murray, E. A. & Fellows, L. K. Prefrontal cortex interactions with the amygdala in primates.  
403 *Neuropsychopharmacol.* **47**, 163–179 (2022).
- 404 16. Johnson, A. W., Gallagher, M. & Holland, P. C. The Basolateral Amygdala Is Critical to the  
405 Expression of Pavlovian and Instrumental Outcome-Specific Reinforcer Devaluation Effects.  
406 *J. Neurosci.* **29**, 696–704 (2009).
- 407 17. Rhodes, S. E. V. & Murray, E. A. Differential Effects of Amygdala, Orbital Prefrontal Cortex,  
408 and Prelimbic Cortex Lesions on Goal-Directed Behavior in Rhesus Macaques. *J. Neurosci.*  
409 **33**, 3380–3389 (2013).
- 410 18. Carmichael, S. T. & Price, J. L. Connectional networks within the orbital and medial  
411 prefrontal cortex of macaque monkeys. *Journal of Comparative Neurology* **371**, 179–207  
412 (1996).
- 413 19. Rockland, K. S. Axon Collaterals and Brain States. *Front. Syst. Neurosci.* **12**, (2018).
- 414 20. Rockland, K. S. What we can learn from the complex architecture of single axons. *Brain*  
415 *Struct Funct* **225**, 1327–1347 (2020).
- 416 21. Kebuschull, J. M. & Zador, A. M. Cellular barcoding: lineage tracing, screening and beyond.  
417 *Nat Methods* **15**, 871–879 (2018).
- 418 22. Han, Y. *et al.* The logic of single-cell projections from visual cortex. *Nature* **556**, 51–56  
419 (2018).
- 420 23. Chen, X. *et al.* High-Throughput Mapping of Long-Range Neuronal Projection Using In Situ  
421 Sequencing. *Cell* **179**, 772–786.e19 (2019).
- 422 24. Gergues, M. M. *et al.* Circuit and molecular architecture of a ventral hippocampal network.  
423 *Nature Neuroscience* 1–9 (2020) doi:10.1038/s41593-020-0705-8.



- 424 25. Russchen, F. T., Bakst, I., Amaral, D. G. & Price, J. L. The amygdalostriatal projections in the  
425 monkey. An anterograde tracing study. *Brain Research* **329**, 241–257 (1985).
- 426 26. Höistad, M. & Barbas, H. Sequence of information processing for emotions through  
427 pathways linking temporal and insular cortices with the amygdala. *Neuroimage* **40**, 1016–  
428 1033 (2008).
- 429 27. Aggleton, J. P., Wright, N. F., Rosene, D. L. & Saunders, R. C. Complementary Patterns of  
430 Direct Amygdala and Hippocampal Projections to the Macaque Prefrontal Cortex. *Cereb*  
431 *Cortex* **25**, 4351–4373 (2015).
- 432 28. Sharma, K. K., Kelly, E. A., Pfeifer, C. W. & Fudge, J. L. Translating Fear Circuitry: Amygdala  
433 Projections to Subgenual and Perigenual Anterior Cingulate in the Macaque. *Cerebral*  
434 *Cortex* bhz106 (2019) doi:10.1093/cercor/bhz106.
- 435 29. Timbie, C. & Barbas, H. Pathways for Emotions: Specializations in the Amygdalar,  
436 Mediodorsal Thalamic, and Posterior Orbitofrontal Network. *J. Neurosci.* **35**, 11976–11987  
437 (2015).
- 438 30. Bassett, D. S. & Bullmore, E. T. Small-World Brain Networks Revisited. *Neuroscientist* **23**,  
439 499–516 (2017).
- 440 31. Park, J. & Moghaddam, B. Impact of anxiety on prefrontal cortex encoding of cognitive  
441 flexibility. *Neuroscience* **345**, 193–202 (2017).
- 442 32. Goldstein, R. Z. & Volkow, N. D. Drug Addiction and Its Underlying Neurobiological Basis:  
443 Neuroimaging Evidence for the Involvement of the Frontal Cortex. *AJP* **159**, 1642–1652  
444 (2002).
- 445 33. Carmichael, S. T. & Price, J. L. Architectonic subdivision of the orbital and medial prefrontal  
446 cortex in the macaque monkey. *Journal of Comparative Neurology* **346**, 366–402 (1994).
- 447 34. Monosov, I. E. & Rushworth, M. F. S. Interactions between ventrolateral prefrontal and  
448 anterior cingulate cortex during learning and behavioural change. *Neuropsychopharmacol.*  
449 **47**, 196–210 (2022).
- 450 35. Wallis, C. U., Cardinal, R. N., Alexander, L., Roberts, A. C. & Clarke, H. F. Opposing roles of  
451 primate areas 25 and 32 and their putative rodent homologs in the regulation of negative  
452 emotion. *PNAS* **114**, E4075–E4084 (2017).

- 453 36. Rudebeck, P. H., Saunders, R. C., Lundgren, D. A. & Murray, E. A. Specialized  
454 Representations of Value in the Orbital and Ventrolateral Prefrontal Cortex: Desirability  
455 versus Availability of Outcomes. *Neuron* **95**, 1208–1220.e5 (2017).
- 456 37. Padoa-Schioppa, C. & Conen, K. E. Orbitofrontal Cortex: A Neural Circuit for Economic  
457 Decisions. *Neuron* **96**, 736–754 (2017).
- 458 38. West, M. J., Slomianka, L. & Gundersen, H. J. G. Unbiased stereological estimation of the  
459 total number of neurons in the subdivisions of the rat hippocampus using the optical  
460 fractionator. *The Anatomical Record* **231**, 482–497 (1991).
- 461 39. Haber, S. N., Liu, H., Seidlitz, J. & Bullmore, E. Prefrontal connectomics: from anatomy to  
462 human imaging. *Neuropsychopharmacol.* 1–21 (2021) doi:10.1038/s41386-021-01156-6.
- 463 40. Trambaiolli, L. R. *et al.* Anatomical and functional connectivity support the existence of a  
464 salience network node within the caudal ventrolateral prefrontal cortex. *eLife* **11**, e76334  
465 (2022).
- 466 41. Fujimoto, A. *et al.* Resting-State fMRI-Based Screening of Deschloroclozapine in Rhesus  
467 Macaques Predicts Dosage-Dependent Behavioral Effects. *J. Neurosci.* **42**, 5705–5716  
468 (2022).
- 469 42. Timbie, C., García-Cabezas, M. Á., Zikopoulos, B. & Barbas, H. Organization of primate  
470 amygdalar–thalamic pathways for emotions. *PLoS Biol* **18**, e3000639 (2020).
- 471 43. van den Heuvel, M. P. & Hulshoff Pol, H. E. Exploring the brain network: A review on  
472 resting-state fMRI functional connectivity. *European Neuropsychopharmacology* **20**, 519–  
473 534 (2010).
- 474 44. Ghashghaei, H. T. & Barbas, H. Neural interaction between the basal forebrain and  
475 functionally distinct prefrontal cortices in the rhesus monkey. *Neuroscience* **103**, 593–614  
476 (2001).
- 477 45. Avendan˜o, C., Price, J. L. & Amaral, D. G. Evidence for an amygdaloid projection to  
478 premotor cortex but not to motor cortex in the monkey. *Brain Research* **264**, 111–117  
479 (1983).
- 480 46. Hiser, J. & Koenigs, M. The multifaceted role of ventromedial prefrontal cortex in emotion,  
481 decision-making, social cognition, and psychopathology. *Biol Psychiatry* **83**, 638–647 (2018).

- 482 47. Myers-Schulz, B. & Koenigs, M. Functional anatomy of ventromedial prefrontal cortex:  
483 implications for mood and anxiety disorders. *Mol Psychiatry* **17**, 132–141 (2012).
- 484 48. Alexander, L. *et al.* Over-activation of primate subgenual cingulate cortex enhances the  
485 cardiovascular, behavioral and neural responses to threat. *Nature Communications* **11**,  
486 5386 (2020).
- 487 49. Alexander, L., Wood, C. M. & Roberts, A. C. The ventromedial prefrontal cortex and emotion  
488 regulation: lost in translation? *The Journal of Physiology* **n/a**,.
- 489 50. Ahmari, S. E. & Dougherty, D. D. Dissecting Ocd Circuits: From Animal Models to Targeted  
490 Treatments. *Depression and Anxiety* **32**, 550–562 (2015).
- 491 51. Huang, L. *et al.* BRICseq Bridges Brain-wide Interregional Connectivity to Neural Activity and  
492 Gene Expression in Single Animals. *Cell* **182**, 177-188.e27 (2020).
- 493 52. Zador, A. M. A critique of pure learning and what artificial neural networks can learn from  
494 animal brains. *Nature Communications* **10**, 3770 (2019).
- 495 53. Cox, R. W. AFNI: Software for Analysis and Visualization of Functional Magnetic Resonance  
496 Neuroimages. *Computers and Biomedical Research* **29**, 162–173 (1996).
- 497 54. Schneider, C. A., Rasband, W. S. & Eliceiri, K. W. NIH Image to ImageJ: 25 years of image  
498 analysis. *Nat Methods* **9**, 671–675 (2012).
- 499 55. Saunders, R. C., Aigner, T. G. & Frank, J. A. Magnetic resonance imaging of the rhesus  
500 monkey brain: use for stereotactic neurosurgery. *Exp Brain Res* **81**, 443–446 (1990).
- 501 56. Harris, C. R. *et al.* Array programming with NumPy. *Nature* **585**, 357–362 (2020).
- 502 57. Pedregosa, F. *et al.* Scikit-learn: Machine Learning in Python. *Journal of Machine Learning*  
503 *Research* **12**, 2825–2830 (2011).
- 504 58. Hunter, J. D. Matplotlib: A 2D Graphics Environment. *Computing in Science & Engineering* **9**,  
505 90–95 (2007).
- 506 59. Waskom, M. L. seaborn: statistical data visualization. *Journal of Open Source Software* **6**,  
507 3021 (2021).
- 508 60. Reveley, C. *et al.* Three-Dimensional Digital Template Atlas of the Macaque Brain. *Cereb*  
509 *Cortex* **27**, 4463–4477 (2017).

- 510 61. Jung, B. *et al.* A comprehensive macaque fMRI pipeline and hierarchical atlas. *NeuroImage*  
511 **235**, 117997 (2021).
- 512 62. Saleem, K. S. *et al.* High-resolution mapping and digital atlas of subcortical regions in the  
513 macaque monkey based on matched MAP-MRI and histology. *NeuroImage* **245**, 118759  
514 (2021).
- 515 63. Hartig, R. *et al.* The Subcortical Atlas of the Rhesus Macaque (SARM) for neuroimaging.  
516 *NeuroImage* **235**, 117996 (2021).
- 517 64. Etzel, J. A., Zacks, J. M. & Braver, T. S. Searchlight analysis: Promise, pitfalls, and potential.  
518 *NeuroImage* **78**, 261–269 (2013).
- 519

## 520 **Methods**

### 521 ***Subjects***

522 Two male rhesus monkeys (*Macaca mulatta*) and one male long-tailed macaque  
523 (*Macaca fascicularis*), 8-9 years of age, were used for our experiments, weighing between 10  
524 and 15 kg. The two rhesus macaques were used in MAPseq experiments whereas the long-  
525 tailed macaque was used in retro-AAV tracing experiments. Animals were housed individually  
526 and kept on a 12-hour light/dark cycle. Food was provided daily with water *ad libitum*.  
527 Environmental enrichment was provided daily, in the form of play objects or small food items.  
528 All procedures were approved by the Icahn School of Medicine IACUC and were carried out in  
529 accordance with NIH standards for work involving non-human primates.

### 530 ***Virus prep***

531 Modified sindbis virus for MAPseq was obtained from the MAPseq Core Facility at Cold  
532 Spring Harbor Laboratory<sup>7</sup>. The viral library used in this study had a diversity of 20,000,000  
533 unique barcodes. Retro-AAV2 coding for mCherry (pAAV2-hSyn-mCherry, Addgene #114472, 2 x  
534 10<sup>13</sup> GC/ml) and green fluorescent protein (pAAV2-hSyn-eGFP, Addgene #50465, 2.2 x 10<sup>13</sup>  
535 GC/ml) under the human synapsin promoter were obtained from Addgene. All viruses were  
536 stored at -80°C and aliquots were thawed over wet ice immediately prior to injection.

### 537 ***Surgery and perfusion***

#### 538 *Sindbis virus injections*

539 For each animal, T1-weighted MRIs were obtained on a Skyra 3T scanner (Siemens) for  
540 surgical targeting. Animals were anesthetized with 5 mg/kg ketamine and 0.015 mg/kg  
541 dexmedetomidine; anesthesia was maintained with isoflurane as needed for the duration of  
542 the scan. Animals were scanned using an MRI-compatible stereotaxic frame (Jerry-Rig, Inc.). 3-4  
543 images were obtained per scan, which were subsequently averaged together using the AFNI  
544 software suite (NIH)<sup>53</sup>. Then, stereotactic coordinates for the BLA could be computed using  
545 ImageJ (NIH)<sup>54</sup>. Two injection tracks were planned to target the middle of the amygdala's

546 anterior/posterior extent, equally spaced in the medial/lateral plane. One anterior injection  
547 track was also planned 1.5 mm in front of the middle of the amygdala, centered in the  
548 medial/lateral plane. Within each track, 4-5 injections 1.5 mm apart were planned in the  
549 dorsal/ventral plane to cover the entire extent of the basal and accessory amygdala nuclei.

550         After allowing approximately one week to elapse after the MRI, anesthesia was induced  
551 using ketamine and dexmedetomidine and maintained with isoflurane as described above.  
552 Surgery was performed under aseptic conditions, using the toothmarker method<sup>55</sup> to place the  
553 animals in the same 3D position as the MRI. The skin, fascia, and muscles were retracted, and  
554 holes were drilled in the skull at each injection location using a surgical drill, widened if  
555 necessary, using rongeurs. Small dural incisions permitted Hamilton syringes access to the brain  
556 surface. 0.4  $\mu$ l of virus was delivered at each injection site at a rate of 0.2  $\mu$ l per minute, after  
557 which the needle was left in place for at least 3 minutes before reaching for the next site.  
558 Injections proceeded from the deepest site to the most superficial. The post-injection wait  
559 period was extended to at least 5 minutes at the top of each injection track before removing  
560 needles from the brain and proceeding to the next track.

561         After all injections were completed, the muscles, fascia, and skin were closed in  
562 anatomical layers. Following surgery, the animal was closely monitored in his home cage until  
563 normal behavior resumed. Postoperative treatment included buprenorphine (0.01 mg/kg, i.m.,  
564 every 8 h) and meloxicam (0.2 mg/kg, i.m., every 24 h), based on attending veterinary guidance,  
565 as well as cefazolin (25 mg/kg, i.m., every 24 h) and dexamethasone sodium phosphate (0.4 –1  
566 mg/kg, every 12–24 h) on a descending dose schedule.

567         Perfusion took place 67-72 hours after the final injection series. After being terminally  
568 anesthetized with ketamine/dexmedetomidine, the animal was prepared for RNase-free  
569 perfusion. All tools were cleaned with RNaseZap solution (Fisher), and all solutions were  
570 prepared using RNase-free reagents. The animal was perfused transcardially with ice-cold 1%  
571 paraformaldehyde (PFA; Electron Microscopy Science) in phosphate-buffered saline (PBS;  
572 Invitrogen) for approximately two minutes, followed by 4% PFA in PBS for approximately 18

573 minutes. Breathing was supplemented by manual ventilation until access to the heart was  
574 obtained.

575 Following brain extraction, the brain was placed in 4% PFA briefly before dissection and  
576 blocking as follows. After the cerebellum was removed, the brain was separated into  
577 hemispheres, the temporal lobes were dissected, and the remaining brain was cut into two  
578 blocks using a cryostat blade: one coronal cut was performed posterior to the central sulcus,  
579 separating the frontal and anterior parietal lobes from the remaining caudal portions of the  
580 brain – ensuring that the thalamus remained in the anterior block. Brain blocks were then post-  
581 fixed in 4% PFA for 48 hours. After post-fix, blocks were frozen slowly over dry ice before being  
582 stored at -80°C until sectioning.

### 583 *Retro-AAV2 injections*

584 Using the same MRI-guided stereotactic approach as above we targeted retro-AAV  
585 injections to the NAcc and AI in the left hemisphere and IOFC and vIPFC in the right hemisphere  
586 of a single monkey. Again, prior to surgery the animal was anesthetized, scanned at 3 T to  
587 obtain structural images, and injection targets were planned based on these scans. On the day  
588 of surgery, the animal was deeply anesthetized and injections were made during an aseptic  
589 neurosurgery. The skin, fascia, and muscles were opened in anatomical layers, burr holes were  
590 drilled over target locations and the dura opened. Injection syringes were then lowered into the  
591 brain and injections of retro-AAV2 were then made into the targets. At each location we  
592 injected 10 µl of virus, at a rate of 0.5 µl per minute. At the conclusion of each set of injections  
593 the needle was left in place for 5 minutes to allow the virus to diffuse. After all injections were  
594 completed, the muscles, fascia, and skin were closed in anatomical layers. Following surgery,  
595 the animal was closely monitored in their home cage until normal behavior resumed.  
596 Postoperative treatment included buprenorphine (0.01 mg/kg, i.m., every 8 h) and meloxicam  
597 (0.2 mg/kg, i.m., every 24 h), based on attending veterinary guidance, as well as cefazolin (25  
598 mg/kg, i.m., every 24 h) and dexamethasone sodium phosphate (0.4 –1 mg/kg, every 12–24 h)  
599 on a descending dose schedule.

600 Eight weeks after surgery, the animals were perfused transcardially with ice-cold 1% PFA  
601 (Electron Microscopy Sciences) in PBS (Invitrogen) for approximately two minutes, followed by  
602 4% PFA in PBS for approximately 18 minutes. The brains were then extracted, postfixed for 24 h  
603 in 4% PFA at 4°C and cryoprotected in 10% glycerol in PBS for 24 h, followed by 20% glycerol in  
604 PBS for another 24 h. The brains were then blocked with one coronal cut posterior to the  
605 thalamus, and the two resulting blocks were frozen in isopentane before storage at -80°C. The  
606 brain was then sectioned in the coronal plane on a freezing stage sliding microtome (Leica) at  
607 40 µm in a 1:8 series. Tissue sets were stored either in PBS with 0.1% sodium azide (Sigma) at  
608 4°C or in cryoprotectant comprised of glycerol, ethylene glycol, PBS, and distilled water  
609 (30/30/10/30 v/v/v/v, respectively) at -80°C.

### 610 ***Sectioning and dissection***

611 From brains injected with sindbis virus, tissue was sectioned at 200 µm on a Leica 3050S  
612 cryostat that had been cleaned with RNaseZap prior to use. Sections were collected over dry ice  
613 and stored at -80°C prior to dissection. Cortical areas were then dissected according to sulcal  
614 landmarks over dry ice. The areas that were collected and our operational definitions of their  
615 boundaries can be found in this table.

Brain Region	Abbreviation	Brodmann's Areas	A/P boundaries	M/L boundaries
Amygdala	n/a		All nuclei across entire A/P extent	
Entorhinal cortex	ento		From the anterior tip to a point adjacent to the mid-hippocampus.	
Hippocampus	HC		Anterior tip to the middle of hippocampus	
Medial orbitofrontal cortex	mOFC	11m, 13a/b, 14	From emergence of medial orbital sulcus to its disappearance	Between rostral sulcus and medial orbital sulcus



Lateral orbito-frontal cortex	lOFC	11l, 12m/r, 13m/l	From emergence of lateral orbital sulcus to its disappearance	Between medial and lateral orbital sulci
Ventrolateral prefrontal cortex	vlPFC	45, 12o, 12l	From emergence of lateral orbital sulcus to its disappearance	Between lateral orbital sulcus and midpoint of laterally extending white matter
Dorsal anterior cingulate cortex	dACC	24	From emergence of cingulate sulcus until area 25 disappears from medial wall/emergence of septum.	Dorsal and ventral banks of cingulate sulcus
Subcallosal anterior cingulate cortex	scACC	25		Medial surface, ventral to corpus callosum, medial/dorsal to medial orbital sulcus
Perigenual anterior cingulate cortex	pgACC	32/24	Anterior to corpus callosum	Cortex on medial surface of the frontal lobe between the rostral sulcus and the cingulate sulcus
Dorsal premotor cortex	PMd	6	Posterior to emergence of arcuate sulcus	Between arcuate and central sulci on dorsal surface
Caudate	n/a			
Putamen	n/a			
Nucleus Accumbens	NAcc		Posterior to emergence of circular sulcus, forming dorsal aspect of insula	ventromedial portion of striatum

Agranular Insula	AI		Orbital surface after disappearance of medial and lateral orbital sulci	From medial corner of orbital surface to where fundus of lateral sulcus used to be
Insula	n/a		From anterior commissure meeting midline	Only cortical surface in depth of lateral fissure
Medial dorsal thalamus	MD		Begins at mid-hippocampus level	Midline nuclei dorsal to midbrain

616

617 Samples from each area were combined across 3 sections in the anterior/posterior plane into  
618 1.5-ml Eppendorf tubes, which were stored at -80°C prior to shipping frozen on dry ice for  
619 sequencing.

#### 620 ***mRNA sequencing and preprocessing***

621 Sequencing of MAPseq projections was performed by the MAPseq Core Facility at CSHL  
622 as described in Kechschull et al. 2016<sup>7</sup>. Briefly, sections were homogenized and treated with  
623 protease before RNA extraction. Total RNA was extracted using an established Trizol-based  
624 protocol. RNA quality was verified on Bioanalyzer and bulk amounts of barcodes were  
625 examined by qPCR and compared with the amount of housekeeping gene prior to sequencing.  
626 Barcode RNA was reverse transcribed into cDNA, and a known amount of RNA (spike-in  
627 sequence) was added to each sample during reverse transcription. Barcode cDNA was then  
628 double-stranded, PCR amplified to produce a sequencing library, and the purified barcode  
629 library was then submitted for a paired-end36 run on an Illumina NextSeq machine.

630 Preprocessing was performed by CSHL using MATLAB (Mathworks) to create a barcode  
631 matrix with size (n samples x n barcodes). Corresponding barcode sequences and spike-in  
632 counts are also extracted to allow for normalization and assessment of duplicates.

#### 633 ***Filtering and analysis***

634           Filtering was performed in Python 3.9<sup>56-59</sup> using a modification of the publicly available  
635 normBCmat.m script<sup>7</sup>; specific analyses can be found in the code available on Github. Briefly,  
636 for each animal, barcodes are filtered, then the raw barcode counts are divided by the spike-in  
637 counts for normalization; barcodes survive filtering if the max barcode amount is found in the  
638 injection sites (amygdala), the max count is greater than 20, and if any other sample (whether  
639 within amygdala or outside) has greater than 5 barcode counts. This adaptation from the  
640 original filtering allows barcodes which send their strongest projections only within amygdala to  
641 survive filtering.

642           The resulting barcode matrix was then binarized and collapsed within brain regions: if a  
643 barcode was found in any of the multiple samples for each brain area, then we counted that  
644 neuron as projecting to that brain area. This collapsing and binarization allowed us to combine  
645 the results from the four sequencing runs: each of the two hemispheres from one animal, and  
646 one hemisphere sequenced twice from the other animal. Only unique barcodes from the re-  
647 sequencing were included in analyses; duplicates were removed based on their barcode  
648 sequences. This filtered, binarized, and collapsed matrix combined across the four hemispheres  
649 was the basis for all analyses in this study.

### 650           *Population summary*

651           Projection proportions were calculated by summing the barcodes found in one brain  
652 area and dividing by the total number of barcodes in the dataset; chance level was defined as  
653 the barcode proportion found in control sites collected from cerebellum. The number of targets  
654 for each neuron is calculated by summing the number of areas in which individual barcodes  
655 were found and subtracting one, to count the number of non-amygdala targets for each  
656 neuron; thus, a neuron which projects from one amygdala sample to another was defined as  
657 having zero targets.

### 658           *Conditional probabilities*

659           To calculate the conditional probability of a neuron projecting to two areas, A and B, we  
660 first found all of the cells that projected to area A (irrespective of their other targets). Then, we

661 found the subset of those cells which also project to area B. Thus, the conditional probability of  
662  $B|A$  is the number of cells that project to both A and B divided by the number of cells that  
663 project to A.

#### 664 ***K-means clustering***

665 We performed k-means clustering using *scikit-learn* Python function. The optimal  
666 number of clusters was determined using the elbow method, in which we plotted the number  
667 of clusters against the within-cluster sum of squares. We found  $k=12$  to be optimal. We then  
668 sorted the projection matrices by k-means cluster.

#### 669 ***Over- and under-represented motifs***

670 To assess whether any branching motifs were under- or over- represented compared to  
671 chance, we first constructed a null distribution based on the overall proportion of barcode  
672 found in each area. We assumed that the probability of a neuron branching to two areas, A and  
673 B, would be the product of the independent probabilities of projecting to A and B:  $p(A\&B) =$   
674  $p(A) * p(B)$ . This approach was taken for bi-, tri-, and quadrifurcations. We did not pursue  
675 analysis of neurons with five or more targets, as there were fewer than 100 neurons with each  
676 number of targets, leading to insufficient sample size on which to perform count-based  
677 statistics.

678 Then, we compared our actual barcode counts to the expected null distribution using a  
679 binomial probability test (*scipy.stats.binomtest*). Resulting p-values were FDR-corrected within  
680 each branching degree, and effect sizes were calculated as  $\log_2\left(\frac{\text{observed}}{\text{expected}}\right)$ .

#### 681 ***Network analysis***

682 To compare projections within the medial and ventral frontal cortex, we first isolated  
683 projections to only one, not multiple, of the areas. We defined these networks by comparing  
684 areas on the orbital surface (mOFC, IOFC, vlPFC, AI) to one another and areas on the medial  
685 surface (dACC, pgACC, scACC). First, we computed the degree of overlap within these networks

686 by preparing Venn diagrams of projections specific to the areas and which branched between  
687 them. The proportion of branching within each area was compared using z-tests for  
688 proportions; p-values were adjusted using FDR correction.

689 We then focused on the projections which were specific while excluding any neurons  
690 which projected to multiple areas in the same network. Projection strength to other areas were  
691 calculated as described above and compared using pairwise z-tests for proportions and Fisher's  
692 exact tests, corrected for multiple comparisons. Degrees of branching were calculated as  
693 before, and branching was compared between brain areas using a permutation test in which  
694 area labels were shuffled 1000x to generate a null distribution; distributions were then  
695 compared using Chi-squared tests. Clustered projection heatmaps were constructed using  
696 *seaborn.clustermap* with Ward's distance.

#### 697 ***Comparison of neurons across populations***

698 To understand whether projection motifs were reproducible across hemispheres and  
699 across animals, we compared each of our independent sequencing runs to simulated neurons  
700 from a uniform distribution (Extended Data Figure 4). 250 neurons were randomly sampled  
701 from each of the sequencing runs and compared to other runs and to the simulated neurons  
702 using cosine distance.

#### 703 ***Stereology***

704 Tissue for stereology was mounted from PBS onto gelatin coated slides and mounted  
705 and coverslipped using Vectashield Vibrance Antifade aqueous mounting medium (Vector  
706 Labs). Slides were stored in a lightproof slide box at 4°C to prevent fluorophore fading during  
707 analysis.

708 An adjacent series was histochemically stained for acetylcholinesterase (AChE) for more  
709 reliable identification of amygdala boundaries. Tissue was incubated overnight at 4°C in a  
710 solution containing 0.68% sodium acetate (Thermo Scientific), 0.1% copper (II) sulfate (Thermo  
711 Scientific), 0.12% glycine (Thermo Scientific), 0.12% acetylthiocholine iodide (TCI America), and

712 0.003% ethopropazine (Sigma Aldrich). The following morning, sections were rinsed 3x in PBS  
713 for 5 minutes each, transferred to a solution of 0.1 M acetic acid (LabChem) with 1% sodium  
714 sulfide (Thermo Scientific) for 1-2 minutes, and then rinsed again 3x with PBS before mounting  
715 as above.

716 Stereology was performed using a Zeiss Apotome.2 microscope equipped with a Q-  
717 Imaging digital camera, motorized stage, and Stereo Investigator software (MBF Bioscience). A  
718 total of 12 sections were used for stereology, evenly distributed to cover the anterior-posterior  
719 extent of the amygdala. The borders of the amygdala were identified using a 5x objective on  
720 the AChE-stained sections, then ROI contours were realigned with the unstained sections for  
721 stereological analysis. EGFP-, mCherry-, and double-labelled cells were counted based on the  
722 soma as the counting target; the optical fractionator probe was used for stereological  
723 estimation as described in West et al., 1991<sup>38</sup>. Neurons were counted under a 10x objective,  
724 with a counting frame of size 150 x 150 x 15  $\mu\text{m}$ ; a 5- $\mu\text{m}$  guard was applied to the dorsal aspect  
725 of each section and a 20- $\mu\text{m}$  guard to the ventral side. Counting frames were arranged in a  
726 670.8 x 670.8  $\mu\text{m}$  grid for systematic-random sampling. Results of the stereological analysis  
727 were compared using z-tests for proportions.

## 728 ***fMRI analysis***

729 Functional connectivity analyses were conducted on a previously published resting-state  
730 functional MRI dataset<sup>41</sup>. We re-analyzed a subset of the scans, including data from 6 rhesus  
731 macaques (5 males), focusing only on the control and pre-injection scans. After performing  
732 standard preprocessing and warping all the brains to a standard template, masks for target  
733 areas were drawn according to the areal boundaries used for MAPseq utilizing the D99,  
734 CHARM, and SARM atlases as a basis<sup>60-63</sup>. Then, functional connectivity was computed between  
735 each amygdala voxel and each target voxel in the ipsilateral hemisphere<sup>64</sup>. Correlations were z-  
736 transformed, and all animals' data was combined into one large dataset after computing  
737 within-animal z-scores. This way, we could analyze all of the amygdala voxels from each animal  
738 without averaging across animals. The following analyses utilized the voxel-wise connectivity  
739 matrix. Whole brain functional connectivity for the amygdala was calculated by averaging the

740 time-series within the anatomically defined amygdala and then correlating the average time  
741 series with every voxel within the brain, for each animal, before averaging across animals.

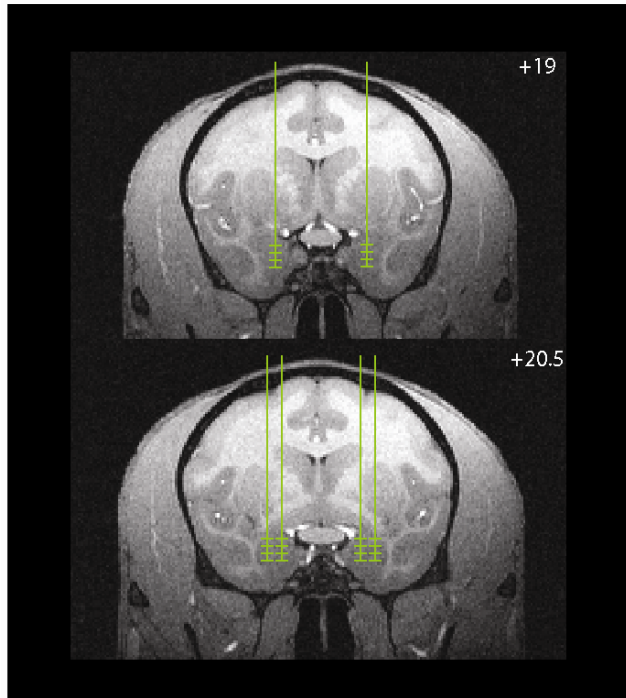
742         The continuous measure of functional connectivity was binarized as follows. For each  
743 amygdala voxel, the peak target connectivity was found; other target voxels which had  
744 connectivity z-scores within 70% of that maximum were said to be connected, while those  
745 under that threshold were said to not be connected. That 70% threshold allows about 5% of the  
746 target voxels to survive filtering (**Supplemental Figure 6**). Then, as in MAPseq, we collapsed the  
747 data across voxels within each target area, such that if one voxel in a target area survived  
748 filtering, we concluded that amygdala was ‘functionally connected’ to that area. Then, we  
749 followed a similar analysis pipeline as for the MAPseq data; computing projection strengths by  
750 counting the proportion of voxels in each area to have survived filtering, computing conditional  
751 probabilities, counting the number of ‘targets’ for each voxel, and performing k-means  
752 clustering. We also performed the same network analysis by filtering for voxels connected to  
753 areas in ventral or medial frontal cortex.

#### 754         **Data and Code Availability**

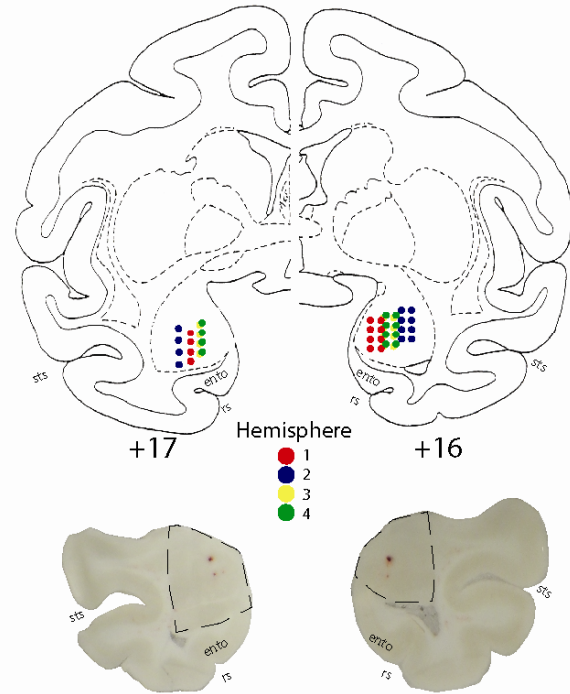
755         Data and code can be made available upon reasonable request by reaching out to  
756 [peter.rudebeck@mssm.edu](mailto:peter.rudebeck@mssm.edu) and [zach.zeisler@icahn.mssm.edu](mailto:zach.zeisler@icahn.mssm.edu).

## Extended Data Figures

A

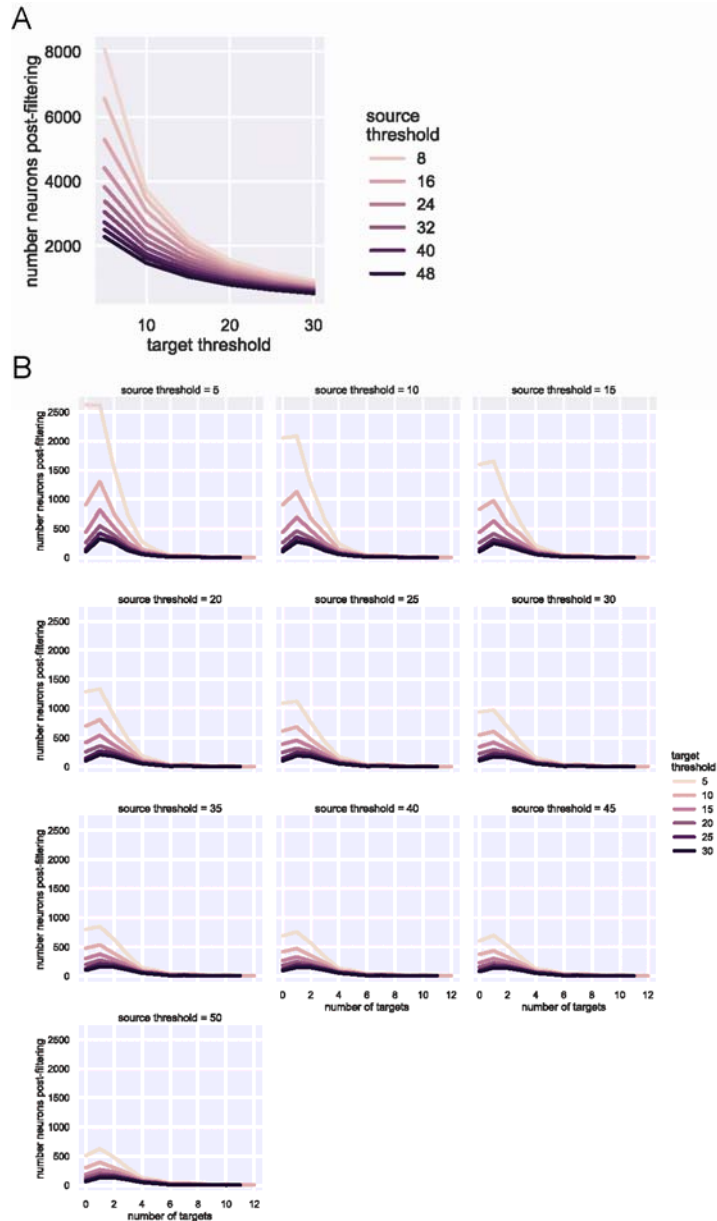


B



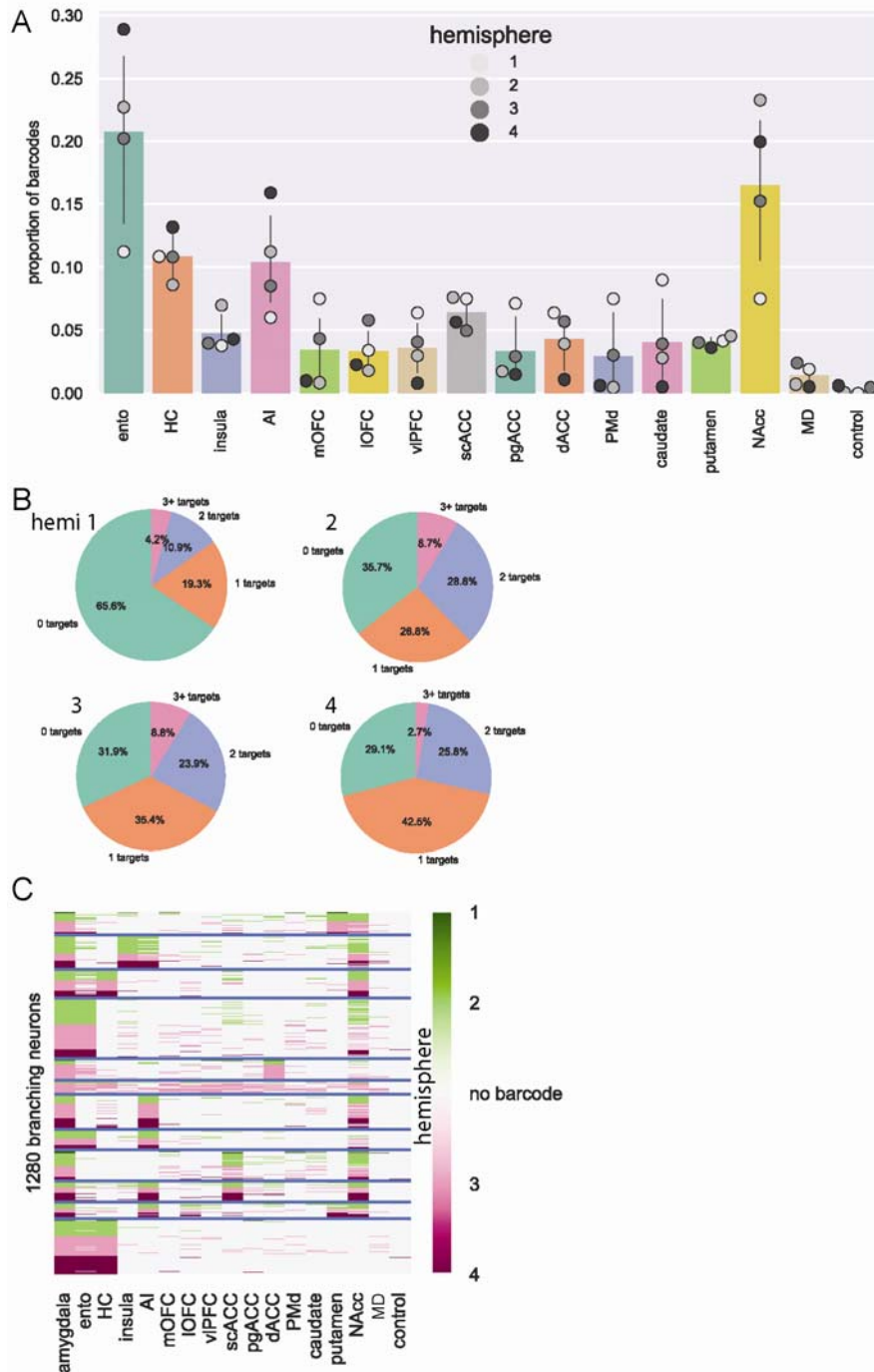
**Extended Data Figure 1: Anatomical verification.** A) Representative MRI images showing anterior (top) and middle (bottom) injection targets within amygdala. Vertical lines indicate intended injection tracks, while horizontal lines indicate injection depths along those tracks. B) Locations of injections for individual animals (colors); anterior injection on the left, middle on the right. Example tissue sections shown below with the extent of the amygdala surrounded by the dotted line (ento refers to entorhinal cortex, rs rhinal sulcus, sts superior temporal sulcus).



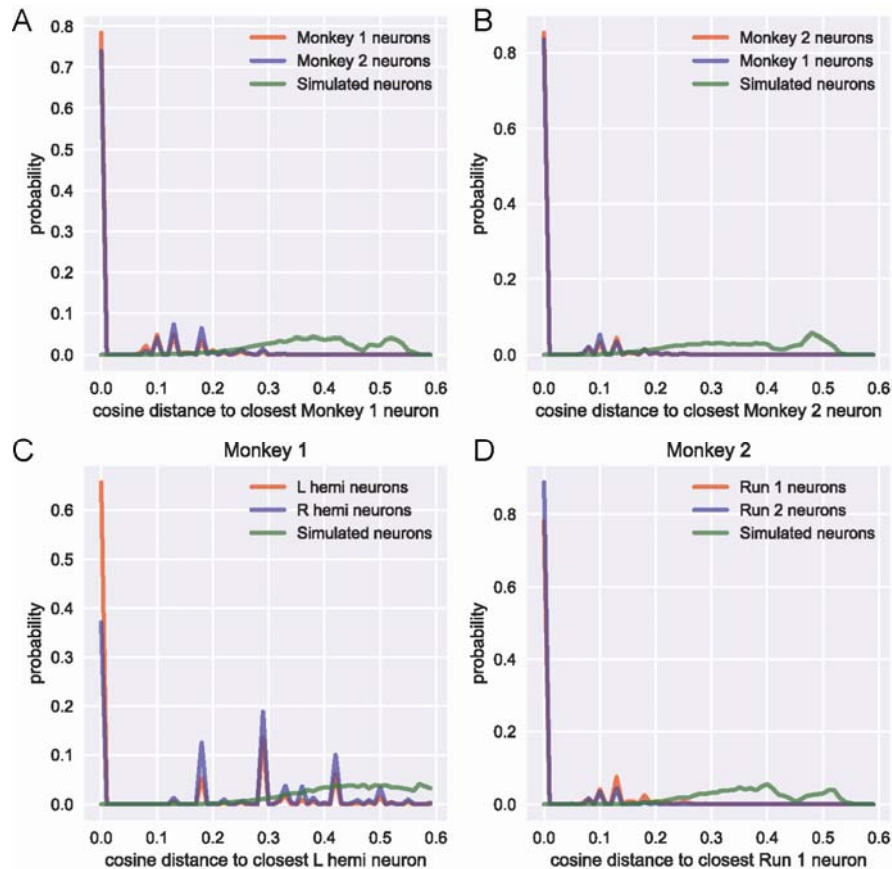


**Extended Data Figure 2. Filtering parameters do not dramatically change recovered barcodes.**

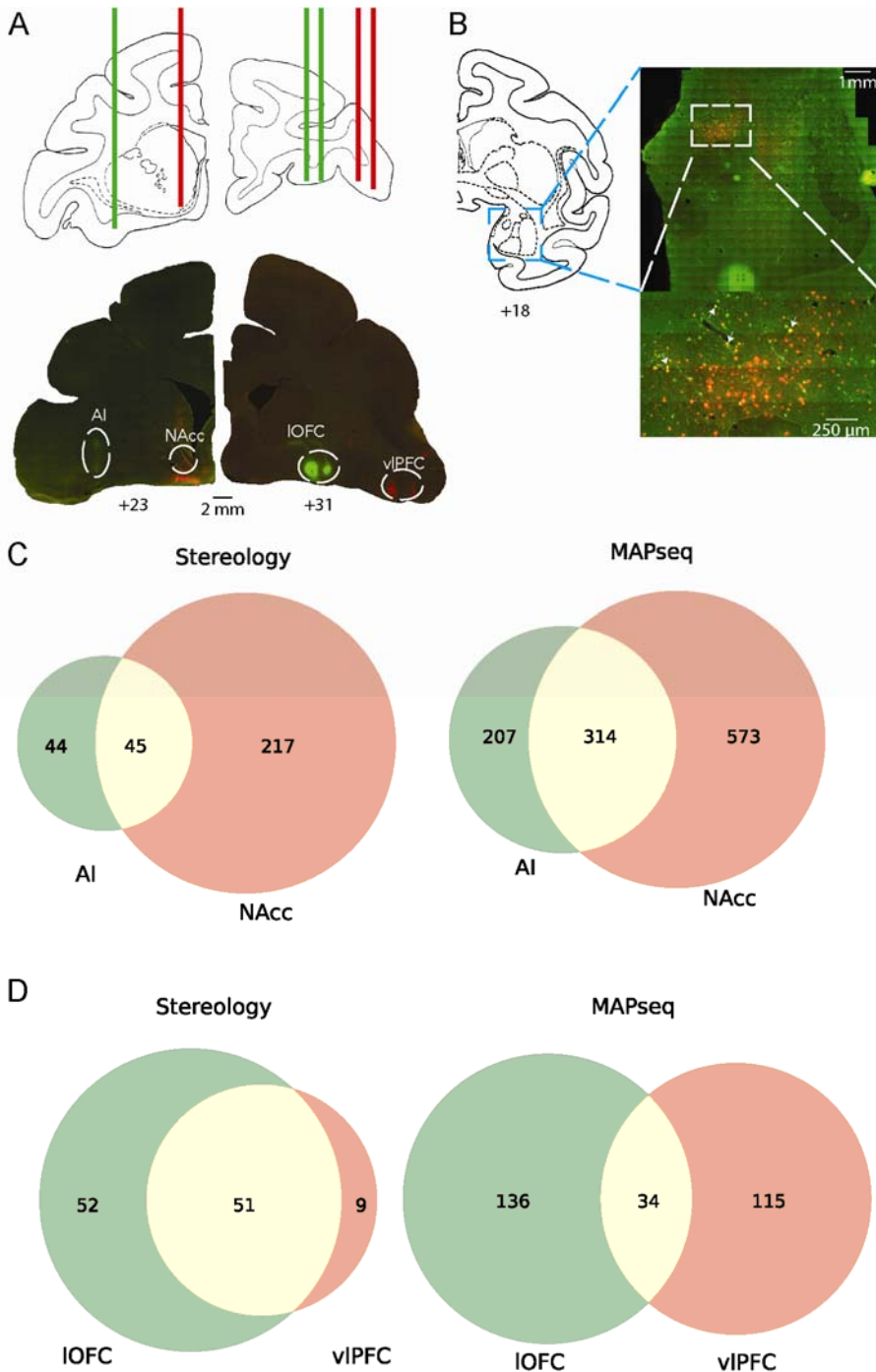
**A)** Number of barcodes surviving filtering for different source thresholds (color of line) and target thresholds (x-axis). Sufficient source threshold eliminates majority of noise. **B)** Effect of thresholding on number of projection targets per neuron. Each plot is one source threshold, while colored lines reflect different target thresholds. The shape of the distributions is lightly flattened by increasing projection threshold, while again, source threshold is responsible for most of the noise.



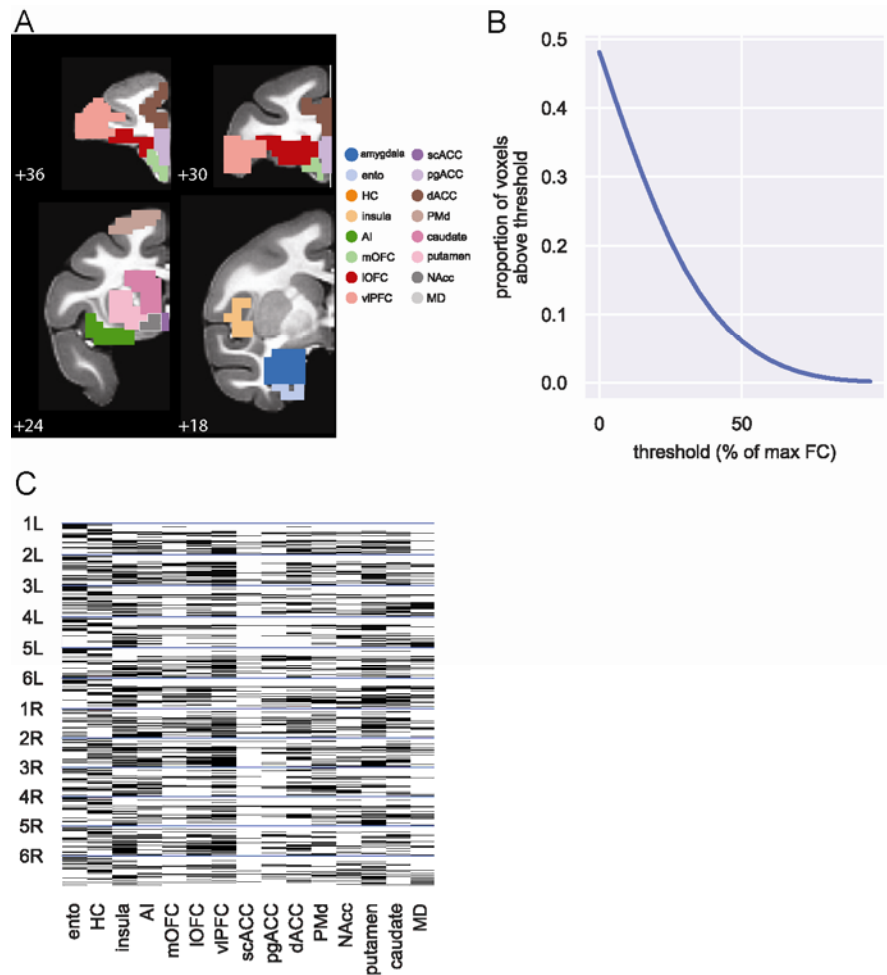
**Extended Data Figure 3: MAPseq is consistent across animals. A)** Overall barcode distribution across areas. Colored bars represent the mean across all 4 hemispheres sequenced, error bars are standard deviation, and individual points reflect counts within each hemisphere's data separately. **B)** Number of targets for each neuron across hemispheres – roughly equal proportions of 1-target and 2+-target neurons, with most variance observed in proportion of 0-target neurons. **C)** K-means clustered branching projections, labelled by hemisphere. Note that most clusters are comprised of neurons from multiple hemispheres.



**Extended Data Figure 4: Comparison across hemispheres.** Density plot of cosine distance between two actual samples (red/blue) and simulated neurons from a uniform distribution (green). **A)** Monkey 1 neurons (both hemispheres) as a basis are more similar to monkey 2's neurons (Kolmogorov-Smirnov test,  $D = 0.12$ ,  $p = 0.81$ ) than the simulated neurons ( $D = 0.52$ ,  $p < 0.0001$ ). **B)** Same for monkey 2 as a basis. **C)** Within monkey 1, the two hemispheres are more similar to each other ( $D = 0.18$ ,  $p = 0.27$ ) than the random neurons ( $D = 0.43$ ,  $p < 0.0001$ ). **D)** Within monkey 2, the two sequencing runs were more similar to each other ( $D = 0.22$ ,  $p = 0.12$ ) than the simulated neurons ( $D = 0.48$ ,  $p < 0.0001$ ).



**Extended Data Figure 5: Stereological confirmation of branching motifs. A)** Top: injection strategy plotted on atlas sections (distances from intra-aural plane in mm); red and green lines refer to mCherry and EGFP retro-AAVs. Bottom: photomicrographs of actual injections sites. **B)** Example retrograde labelling in amygdala (shown in atlas on right). The bottom image is comprised of approximately 4x4 tiled 10x magnified images. Double labelled cells are non-exhaustively labelled with arrows. **C)** Stereology results (left) from left hemisphere injections compared to MAPseq results (right). **D)** Same for right hemisphere injections.



**Extended Data Figure 6: fMRI analysis.** **A)** ROIs used for fMRI analysis shown on NMT atlas slices (hippocampus and MD not shown). **B)** Proportion of voxels determined to be ‘functionally connected’ decreases with increasing threshold (the threshold was set at 70% because ~5% of voxels survive filtering). **B)** Binarized and collapsed MRI connectivity. Number labels refer to individual animals, while L and R refer to left and right hemispheres, respectively; only ipsilateral connections were assessed.